IMPROVED STRAIN ANALYSIS OF LEFT VENTRICULAR FUNCTION POST MYOCARDIAL INFARCTION IN MICE

by

Danielle Wilson

April, 2019

Director of Thesis: Stephanie M. George

Major Department: Engineering

A myocardial infarction (MI), caused by an arterial blockage preventing blood from flowing to a part of the heart, restricts tissue oxygenation and results cell death and myocardial tissue damage. This compromises contractility, resulting either in sudden death, or ventricular remodeling and eventually heart failure. Echocardiography is the standard, non-invasive cardiac imaging technique for humans and small animals. The standard measurements obtained from M-mode echocardiography to assess left ventricle (LV) function lack the sensitivity to detect subtle changes in regional LV performance at the early stages of disease. Speckle tracking techniques in conjunction with strain analysis overcome this issue by tracking the movement of the myocardium across 6 transverse segments of the LV. Analysis of strain in more regions of the heart from the apex (bottom) to base (top) would reveal earlier, localized detection of LV dysfunction.

The purpose of this study is to develop a methodology to improve regional specificity in the analysis of strain and strain rate (SR) relative to the site of injury in mouse hearts in 12 equal segments along the myocardium and compare these results to the VevoStrain software (VisualSonics) strain values. Echocardiographic images obtained from the Vevo 3100

(VisualSonics) ultrasound in uninjured hearts or after acute ischemia/reperfusion (30minI/24hr R) injury induced by ligation of the left anterior descending coronary artery were analyzed using MATLAB (MathWorks). To quantify strain, the motion of the speckles was tracked between the epicardium and endocardium for 3 consecutive cardiac cycles. Perpendicular lines were generated connecting these contours. Displacement of these lines were calculated from the starting location to end location to calculate strain. The LV was divided into 12 equal segments. The peak % strain values across the region of interest were averaged for the 12 segments to obtain global strain measurements. To measure SR, the change in strain was divided by the time between frames. The novel strain analysis was compared to the VevoStrain software data to validate the results. These values were used to measure the contractile function of the LV between sham, MI, and MI+ephrinA1-Fc mice. Feasibility of the proposed algorithm has been demonstrated, but due to some limitations, more work is needed to improve this method. With further work, this method could optimize the treatment process by determining the location being treated and extent of treatment to the infarct and remote regions of the heart.

IMPROVED STRAIN ANALYSIS OF LEFT VENTRICULAR FUNCTION POST MYOCARDIAL INFARCTION IN MICE

A Thesis

Presented to the Faculty of the Department of Engineering

East Carolina University

In Partial Fulfillment of the Requirement for the Degrees

Master of Science in Biomedical Engineering

by

Danielle Wilson

April, 2019

Improved Strain Analysis of Left Ventricular Function Post Myocardial Infarction in Mice

by

Danielle Wilson

APPROVED BY:

DIRECTOR OF
THESIS:_____
Stephanie M. George, PhD

COMMITTEE MEMBER:_____
Jitka Virag, PhD

COMMITTEE MEMBER:_____
Zhen Zhu, PhD

CHAIR OF THE DEPARTMENT

OF ENGINEERING:_____
Barbara Muller-Buller, PhD

DEAN OF THE

GRADUATE SCHOOL:_____
Paul J. Gemperline, PhD

TABLE OF CONTENTS

LIST OF FIGURES

INTRODUCTION

According to the American Heart Association (AHA), cardiovascular disease is the leading cause of death globally, and remains the number one cause of death in the United States (Benjamin et al. 2019; Heusch and Gersh 2016; Gerczuk and Kloner 2012). Cardiovascular disease is defined as any heart condition caused by diseased blood vessels, structural changes, or blood clots. A heart attack is caused by a blockage preventing blood from flowing to a part of the heart, resulting in myocardial cell death. This is referred to clinically as a myocardial infarction (MI). Approximately every 40 seconds an American will have a MI (Benjamin et al. 2019). This killed 114,023 citizens in 2015 (Benjamin et al. 2018). In 2013, MI was one of the 10 most expensive medical conditions treated in hospitals in the United States with a cost of 12.1 billion dollars (Benjamin et al. 2019). Therefore, there is a huge need to improve treatment efficacy to reduce the number of Americans killed by this awful disease and alleviate the socioeconomic burdens.

BACKGROUND RESEARCH

Anatomy

The human heart has four chambers - the right atrium, right ventricle, left atrium, and left ventricle. The right atrium receives deoxygenated blood from the superior and inferior vena cava and pumps it to the right ventricle. Once the right ventricle receives the blood, it pumps the blood to the lungs through the pulmonary artery to become oxygenated. The left atrium receives the oxygenated blood from the lungs and then pumps the blood to the left ventricle. Finally, the left ventricle pumps the oxygen rich blood to the aorta, which delivers blood to the body. This is represented in Figure 1, where the blue areas represent deoxygenated blood, and the red areas represent oxygenated blood.

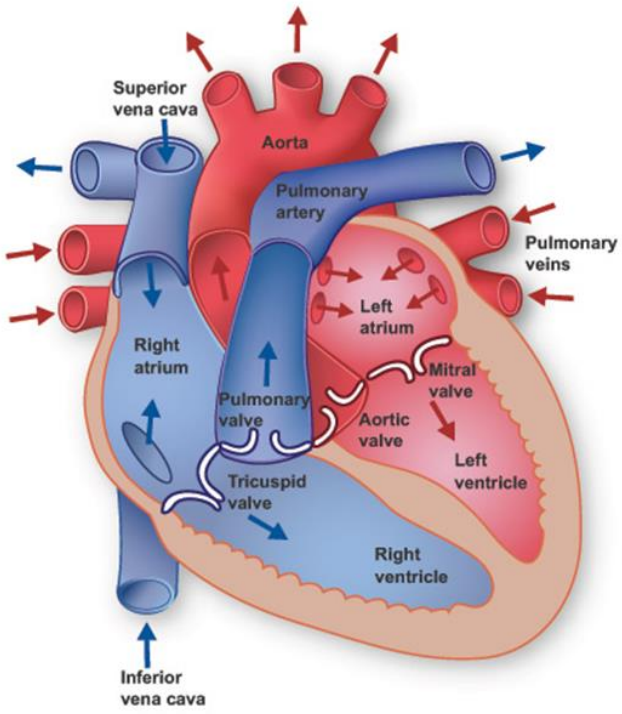

Figure 1 Anatomy of Human Heart (Texas Heart Institute)

The heart has four valves; tricuspid valve, mitral valve, pulmonary valve, and aortic valve. These valves are also shown in Figure 1. The valves regulate and control the one directional flow of

blood through the heart, pulmonary artery, and aorta. The heart also has coronary arteries, the largest of which are conduit vessels that run along the surface of the heart and deliver the oxygen rich blood to the heart muscle. The main coronary arteries of the anterior side of the epicardial can be viewed below in Figure 2. The coronary arteries are vital blood vessels that are responsible for nourishing the heart tissue. A MI is caused by an occlusion of these coronary arteries.

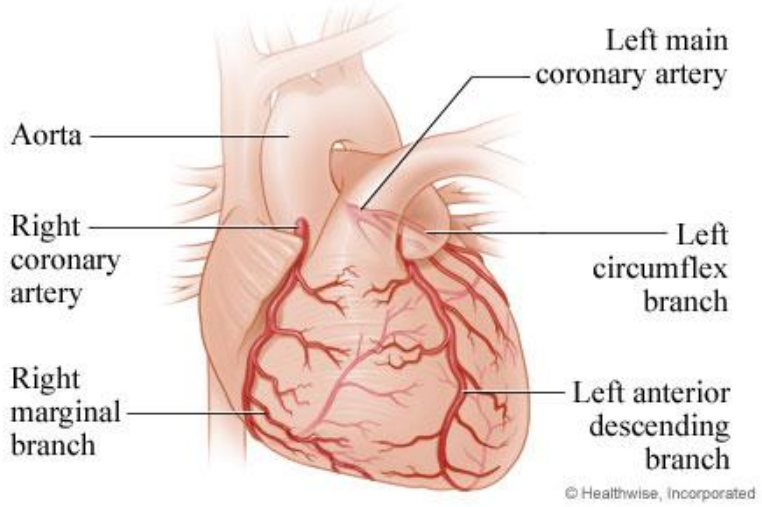

Figure 2 Coronary Arteries (Healthwise)

Epidemiology

Acute MI due to occlusion of an epicardial artery most commonly occurs following rupture of an atherosclerotic plaque, resulting in transmural ischemia (Heusch and Gersh 2016; Klabunde 2011; Thygesen et al. 2012). Myocardial ischemia is the imbalance between oxygen supply and demand (Thygesen et al. 2012). The process of a MI is represented in Figure 3 below. The size and severity of the MI is dependent upon the size of the ischemic area, the duration and intermittency of the occlusion, and the magnitude of collateral blood flow (Heusch and Gersh 2016; Roger 2007; Thygesen 2012; Klabunde 2012). When the flow of blood is blocked to an area of the myocardium, the cardiomyocytes downstream of the occlusion become necrotic as the

cells are no longer provided with oxygen (Dries et al. 2011). Therefore, the contractility of the heart is compromised, resulting either in sudden death, or leading to ventricular remodeling and eventually heart failure (Benjamin et al. 2018; Klabunde 2012; Dries et al. 2011; O'Neal et al. 2013).

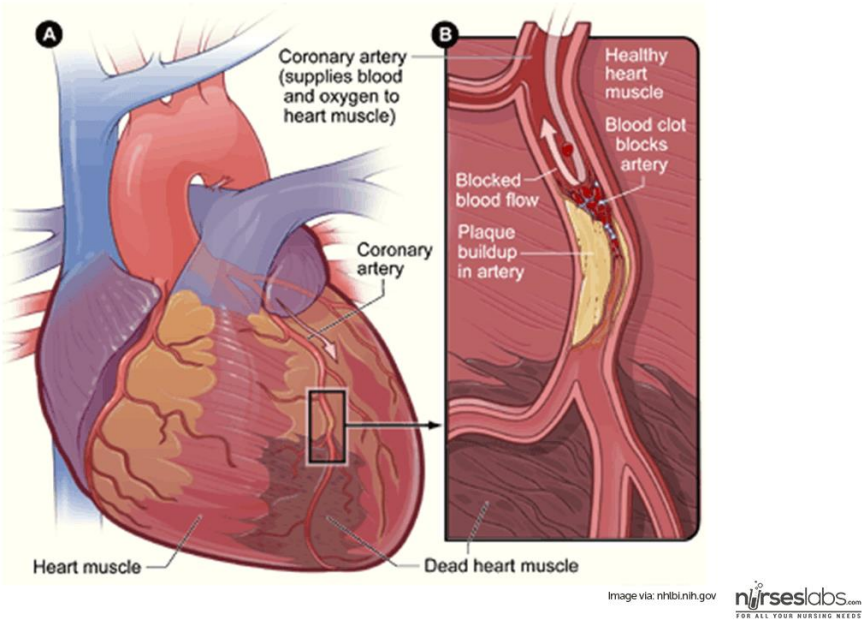

Figure 3 Anatomy of Myocardial Infarction (NIH 2016)

MI can be detected by a trained medical doctor using electrocardiographic (ECG) recordings as the conduction pathway is compromised, and the electrical signal is no longer transmitted across the necrotic cells. Typical ECG changes that are commonly seen as a result of a MI are the presence of ST segment elevations or depressions, T wave inversions, and/or Q waves, displayed below in Figure 4 (Thygesen et al. 2012; Klabunde 2012). In addition, cardiac Troponin 1, which is a serum biomarker released following cardiac cell death, can be measured as an indicator of infarct size (Dries et al. 2011). However, there is variability associated with this due to injury onset and size, and issues with specificity and false negatives.

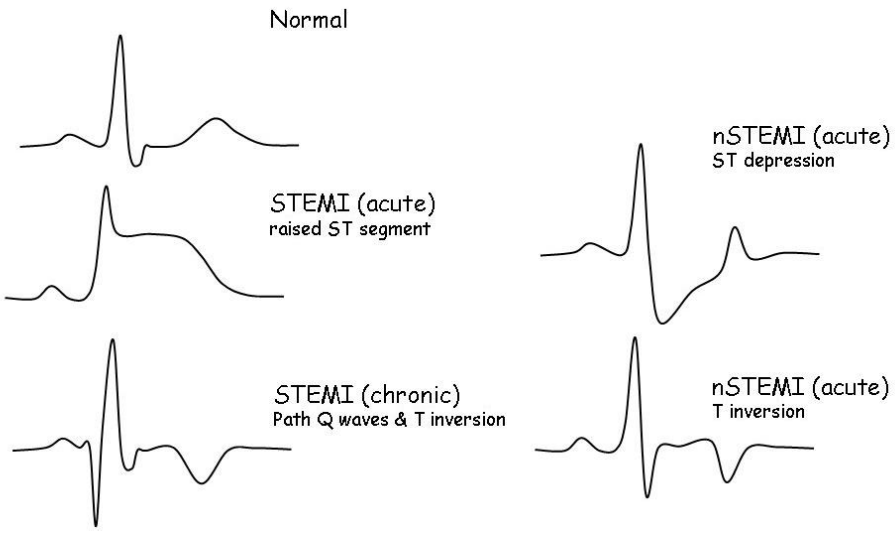

Figure 4 ECG Changes in Myocardial Infarction (Torrens 2016)

Given the heart of a mouse is similar to that of a human, in addition to the relatively low cost of utilizing a mouse model, it is realistic to analyze the effect of MI and treatment after an MI with a mouse model (Ram et al. 2011; Tang et al. 2012). However, it is important to understand the physiological differences of mice compared to adult humans as these differences may impact the results.

Cardiac Physiology in Mice

The mouse heart is much smaller in size with an increased heart rate compared to a human heart (Bhan et al. 2014; Ram et al. 2011; Ferferieva et al. 2012). The size of an adult mouse heart is 5-8mm in length with an average heart rate of 400-650 beats per minute (Lindsey et al. 2018). This requires high spatial and temporal resolutions to properly visualize the structure and physiology of the left ventricle (Ram et al. 2011; Rea et al. 2016).

Like a human heart, a healthy mouse heart should contract as one single contractile unit for the atria and one single unit for the ventricles. When the heart becomes injured, the way the heart

contracts becomes affected. When an area or region of the heart contracts at a different time than the rest of the heart, the contraction is out of sync and thus global cardiac function in terms of output (oxygenated blood) is compromised. Often this is quantified as dyssynchrony of the ventricle based on time to peak strain which is a measure of deformation (Bhan et al. 2014; Ram et al. 2011).

Left Ventricle Dysfunction

Echocardiography Conventional Parameters

Left ventricle (LV) dysfunction often leads to left ventricular remodeling after myocardial injury. Echocardiography is the standard cardiac imaging technique for humans and small animals as it is noninvasive, inexpensive, widely available, and has a short imaging and post-processing time (Bauer et al. 2012; Andrews et al. 2013; Ram et al. 2011; An et al. 2016). The standard measurements obtained from M-mode echocardiography to assess LV function are chamber dimensions, wall thickness, ejection fraction (EF), and fractional shortening (FS) (Andrews et al. 2013; Bauer et al. 2012; Ram et al. 2011; Rea et al. 2016; Theodoropoulos and Xu 2008; Tang et al. 2012). However, these conventional echocardiography measurements lack the sensitivity to detect subtle changes in regional LV performance at the early stages of disease progression (Bauer et al. 2012; Theodoropoulos and Xu 2008; Ferferieva et al. 2012) and are limited by region specific analysis in a particular plane, usually at mid-papillary level. Therefore, new imaging techniques are being developed to improve analysis of LV dysfunction.

Strain/Strain Rate

Utilizing a speckle tracking technique with strain analysis enables the ability to detect subtle changes in LV function after a MI, and may thus provide a window of possibility for treatments that may reduce or at least slow the progression to dysfunction and heart failure. (Bauer et al.

2012; Ferferieva et al. 2014; Andrews et al. 2013; Ram et al. 2011; An et al. 2016). Cardiac abnormalities, with the absence of changes in conventional parameters, can be detected with strain analysis (Andrews et al. 2013). Speckle tracking technique stands out among the rest of echocardiography imaging techniques because this method is angle independent, which is an important feature for a dynamic organ that is continually in motion (Bauer et al. 2012; Bhan et al. 2014; Ferferieva et al. 2012; Theodoropoulos and Xu 2008; Tang et al. 2012; Bachner-Hinenzon et al. 2012; Amundsen et al. 2008). Speckle tracking imaging tracks the movement of the myocardium, based on the speckles generated from the reflection and scattering of the ultrasonic beam, seen along the myocardium on the images (Bhan et al. 2014; Ferferieva et al. 2012; Ram et al. 2011; Rea et al. 2016; Tang et al. 2012; Spurney et al. 2011).

Strain is defined as the change in length divided by the original length,

$$\varepsilon(t) = (L(t) - L_0)/L_0 \quad (1)$$

and strain rate is defined as the rate of change of deformation over time,

$$\frac{d}{dt}\varepsilon(t) = [(L(t) - L_0)/L_0] \times sec^{-1} \quad (2)$$

ε represents the strain, L represents the length between the epicardium to endocardium, and L_0 represents the unstressed length between the epicardium to endocardium.

Commercial algorithms have been generated to calculate the strain and strain rate of the myocardium based on the B-mode images. These algorithms can determine the circumferential, radial, and longitudinal strain and strain rate globally or regionally across six segments of the LV, shown below in Figure 5 (Bauer et al. 2012; Bhan et al. 2014, Ferferieva et al. 2012; Andrews et al. 2013). The six segments for the long axis are posterior base, mid posterior, posterior apex, anterior base, mid anterior, and anterior apex, and the six segments for the short

axis are lateral, posterior, inferior free, posterior septum, anterior septum, and anterior free. Global measurements are equal to the average of the six segments.

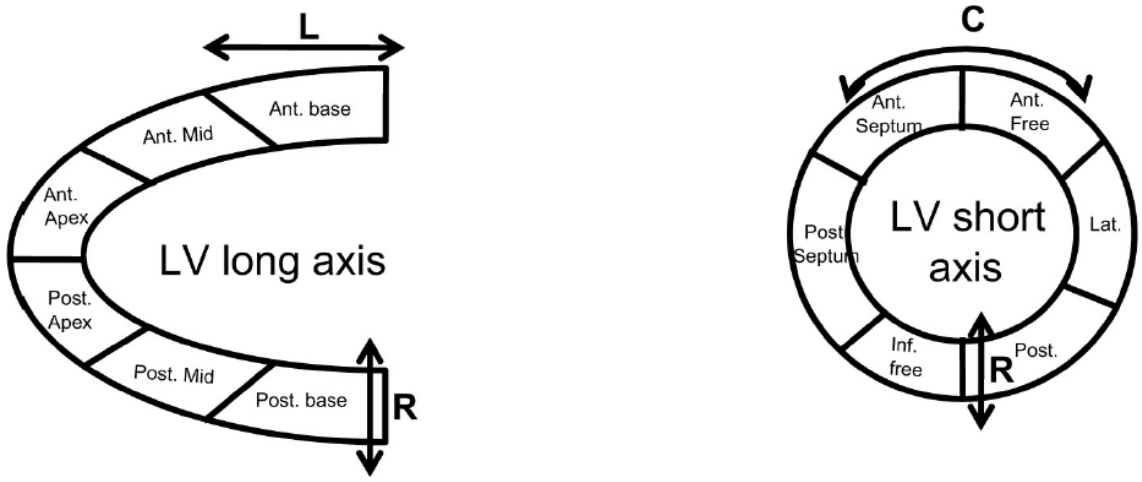

Figure 5 Regions of LV for Strain Assessment (Ram et al. 2011)

Radial and longitudinal strain and strain rate can be measured with long axis images, where radial and circumferential strain and strain rate can be measured with short axis images. The orientation of the heart in regards to the strain measured can be visualized in Figure 6.

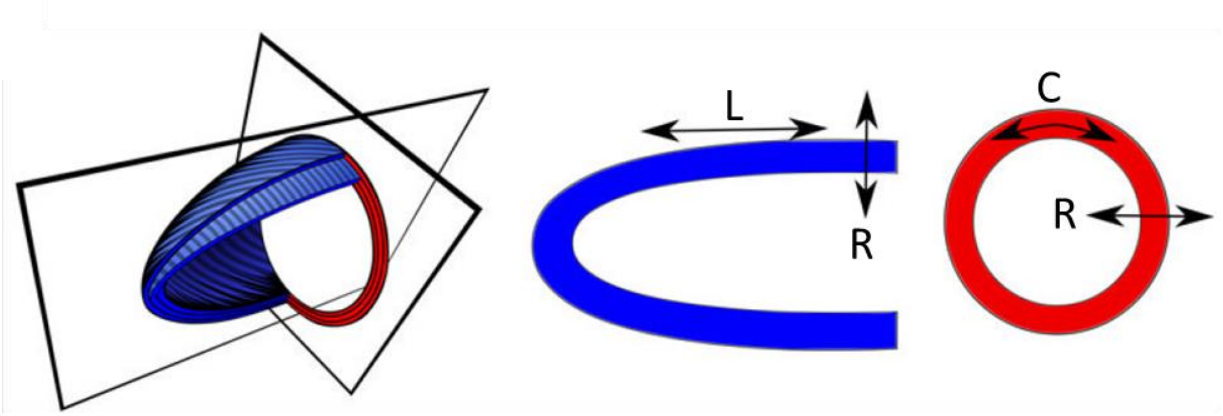

Figure 6 Axis Orientation (L- longitudinal, R- radial, C- circumferential) (Bauer et al. 2012)

Cardiac assessment with murine models is being performed to measure the strain in the heart after injury of the left anterior descending (LAD) artery. Using a high-frequency microultrasound system with speckle tracking (Visualsonics Vevo 2100), researchers are able to detect LV remodeling through strain analysis (VevoStrain) of B-mode images. The endocardium and epicardium are traced semi-automatically, which can be manually adjusted if necessary (Andrews et al. 2013; Bauer et al. 2012; Bhan et al. 2014; Ram et al. 2011). When looking at an MI group compared to sham (control) group of murine models, longitudinal and radial global strain and strain rate were lower for the MI group (radial strain post-MI 7 weeks 7.5 ± 1.5 vs sham 19.9 ± 3.2; longitudinal strain post-MI 7 weeks -3.9 ± 1.2 vs sham -15.4 ± 2) (Bhan et al. 2014; Bauer et al. 2012). In addition, regional strain and strain rate values were lower for the MI group, especially in the apical region of the heart (Bhan et al. 2014). Myocardial performance was decreased for both infarct and non-infarct regions 1 week post-MI (Bauer et al. 2012). Circumferential global strain was reduced early post-MI (Bauer et al. 2012). Dyssynchrony of the LV was significantly increased in the MI group and positively correlated with infarct size (radial dyssynchrony MI $20.4 \pm 2\%$ vs. sham $8.5 \pm 1.4\%$; longitudinal dyssynchrony MI $16.6 \pm 2.2\%$ vs. sham $7.5 \pm 1.3\%$; $P < 0.01$) (Bhan et al. 2014).

A study interested in the feasibility of speckle tracking strain analysis of pediatric mice, used the Vevo 2100 system on groups of healthy pediatric mice at three different ages, as this ultrasound system has only been used for adult mice before. The apical region of the LV resulted in different radial and longitudinal strain and strain rate values compared to mid and basal regions, which was similar to adult mice findings (Andrews et al 2013; Bhan et al. 2014).

In another group using a different software platform with speckle tracking images from GE Vingmed Ultrasound (EchoPAC workstation), the endocardium was manually traced and then

the speckle region of interest width was automatically selected between the endocardium and epicardium (Ferferieva et al. 2012). As expected, the global circumferential strain and strain rate values were lower in the MI group compared to the control group during resting conditions (strain $-5.4 \pm 4.9\%$; strain rate $-2.9 \pm 1.9 s^{-1}$; $P < 0.05$) (Ferferieva et al. 2012). As the strain analysis shows that LV performance decreases from acute MI, the need for a treatment for MI is desperately needed.

Custom-made algorithms have been generated to calculate the strain and strain rate of the heart from B-mode images using MATLAB (MathWorks Inc., Natick, Massachusetts). A study compared the strain in the LV of dogs at baseline and post-MI of the LAD using sonomicrometry with SonoVIEW (Sonometrics corp.). Speckle tracking of the echocardiographic images were performed using a sum of absolute differences method, tracking the speckles along four regions of interest over 3 cardiac cycles (Amundsen et al. 2006; Amundsen et al. 2008). The study validated the speckle tracking method against the strain derived sonomicrometry and MRI method, producing decreased strain values in the occlusion group (Amundsen et al. 2006). A study analyzing the feasibility of cardiac function assessment in vitro vs in vivo in fetal rabbits used a motion estimation algorithm in MATLAB where the speckles in the defined region of interest were tracked across the cardiac cycles to measure the longitudinal and circumferential strain (Zhu et al. 2015). In vitro analysis produced higher longitudinal and radial strain compared to the in vivo study (Zhu et al. 2015).

In addition to animals, studies have been conducted asses cardiac function via strain analysis in humans. Combining the use of echocardiographic data with tissue doppler data, strain and strain rate are being measured (Nakatani et al. 2003; Amundsen et al. 2008). Short-axis echocardiographic images can be obtained at three levels (apical, mid, and basal) of the LV to

get a total of 12 segments (Nakatani et al. 2003; Stefani et al. 2007). Tissue doppler and echocardiogram data were imported into MATLAB to measure wall deformation based on speckle tracking analysis with custom code (Nakatani et al. 2003; Stefani et al. 2007; Amundsen et al 2008). Results indicated significantly different strain rate values for different wall motion classifications (Nakatani et al. 2003). Speckle tracking strain resulted in an overall accuracy of 86% and was found superior compared to only tissue doppler strain (Amundsen et al. 2008). When comparing the longitudinal strain values at the basal segment derived from a tissue doppler method to speckle tracking method, the results were equivalent at around 20% peak longitudinal strain from a 4-chamber imaging view (Stefani et al. 2007).

Magnetic Resonance Imaging

In addition to quantifying LV dysfunction as strain with speckle tracking ultrasound, magnetic resonance imaging (MRI) is being used to quantify functional changes in human and murine hearts. MRI is considered to be the noninvasive gold standard for assessing contractile function and the extent and severity of MI in humans (Chan et al. 2006; Li et al. 2007). It has also been shown to be a reliable cardiac imaging tool for mice (Gilson et al. 2005; Li et al. 2007; Zhou et al. 2003; Epstein et al. 2002). MR images are acquired along the LV from the short axis, shown in Figure 7, and then reconstructed to visualize the whole chamber (Chan et al. 2006; Epstein et al. 2002; Gilson et al. 2005; Li et al. 2007; Zhou et al. 2003; Gerber et al. 2002). With MR tagging, the contractile dysfunction of the LV can be analyzed after a MI of the LAD. Spatial modulation of magnetization (SPAMM) creates bands within the image which can be tracked to measure myocardial strain based on deformation (Zhou et al. 2003; Epstein et al. 2002; Amundsen et al. 2008). Studies have found that the circumferential strain of the injured mice hearts is significantly less than the circumferential strain of the healthy mice hearts (Chan et al.

2006; Gerber et al. 2002; Gilson et al. 2004; Gilson et al. 2005). Studies have also analyzed the severity of the MI with contrast-enhanced (CE) MRI. After an intravenous injection of gadodiamide or gadoversetamide, the region of the MI is visualized to analyze the severity of the necrosis and occlusion (Gerber et al. 2002; Chan et al. 2006). Using a 1.5T scanner, short axis ECG-gated images are obtained after injection of the dye (Chan et al. 2006; Gerber et al. 2002). Immediate imaging after injection showing hypoenhancement of the core of the infarct represents microvascular occlusion, where delayed imaging after injection showing hyperenhancement represents myocardial necrosis (Gerber et al. 2002). The extent of infarction is computed as a percent in signal intensity increase compared to the average (Gilson et al 2004; Gerber et al. 2002). When comparing echocardiogram strain results to CE MRI results, global longitudinal strain was associated with MI size and LV dysfunction (Kim et al. 2017).

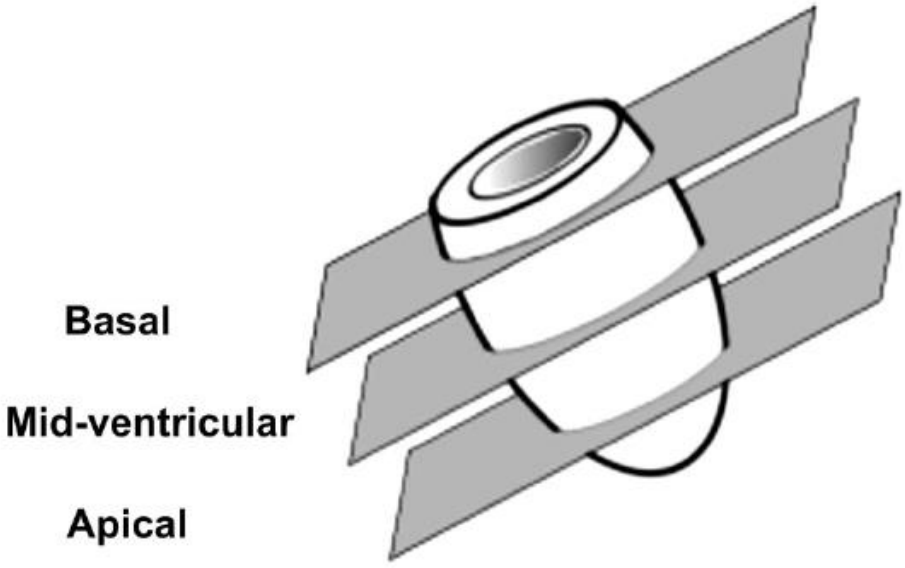

Figure 7 Short Axis Slice Locations of the LV (Gilson et al. 2005)

Although MRI is a highly accurate imaging method to quantify cardiac dysfunction and structure due to its high spatial and contrast resolution, there are several limitations to this modality (Li et

al. 2007; Zhou et al. 2003; Epstein et al. 2002). MRI scanning is very expensive with much slower image acquisition times compared to ultrasound (Li et al. 2007; Gilson et al. 2004). In addition, interslice gaps of the heart occurs leading to incomplete coverage the LV (Gilson et al. 2005). This is due to the slices being separated by 0.5mm, illustrated in the diagram above in Figure 7 (Gilson et al. 2005). There is often high signal-to-noise ratio due to unwanted respiratory motion from breathing or respiratory gating is used due to unavoidable breathing interfering with the imaging (Gilson et al. 2005; Li et al. 2007; Gilson et al. 2004).

Treatment

To prevent the damage after a MI, techniques need to be developed to maintain cardiomyocyte survival, reduce infarct size, and thus reduce LV remodeling (Dries et al. 2011). Since 1986, the standard of care for acute MI is reperfusion therapy to reduce injury, preserve LV function, and decrease mortality (DuSablon et al. 2017; O'Neal et al. 2013). These therapies, such as coronary artery bypass grafting (CABG), must be performed within hours of the ischemic event to slow progressive remodeling; however, they do not restore normal cardiac function (DuSablon et al. 2017; O'Neal et al. 2013). Combining reperfusion techniques with promoting angiogenesis and reducing inflammation immediately after injury, reduces remodeling and LV dysfunction (O'Neal et al. 2013).

Intramyocardial administration of ephrin A1-Fc in mice has been shown to restrict tissue damage after a non-reperfused MI (DuSablon et al. 2017). EphrinA1-Fc is known to have angiogenic properties but the protective effects are unrelated to changes in vascular density (DuSablon et al. 2017; O'Neal et al. 2013; Dries et al. 2011). A study assessing the success of this ephrin A1-Fc treatment compared the LV function in uninjured controls, IgG-Fc-treated controls, and ephrin A1-Fc treated mice after 24 hours and 4 days reperfusion post-MI. The mice treated with IgG-Fc

displayed significant impairment in FS and EF 24 hours and 4 days post-MI compared to uninjured mice (DuSablon et al. 2017). The mice treated with a single injection ephrin A1-Fc experienced no significant differences in FS or EF 24 hours or 4 days post-MI compared to uninjured mice (DuSablon et al. 2017). Histological staining and morphometric analysis found ephrinA1-Fc mice had 46% reduction (DuSablon et al. 2017) and 50% reduction (Dries et al. 2011) in infarct size compared to the IgG-Fc mice. Thus, ephrinA1-Fc administered at time of injury significantly decreased ischemic damage and myocardium dysfunction post-MI (DuSablon et al. 2017; Dries et al. 2011).

Limitations of Current Research

Although there have been recent advances in the assessment and treatment of cardiac function, there are still some limitations that need to be overcome. When acquiring the gray scale images, weak scatter reflections are often lost due to the high signal to noise ratio (Ram et al. 2011; Nakatani et al. 2003). This leads to difficulty in analysis of strain and strain rate measurements. In addition, geometric assumptions are made for the conventional parameters (Ram et al. 2011; Bhan et al. 2014). Tissue doppler derived strain is angle dependent (Stefani et al. 2007). The regional strain analysis is broken down into six segments, where each segment is the entire wall thickness. However, during non-transmural MI, the ischemia first starts at the endocardium (Bachner-Hinenzon et al. 2012). In addition, the ephrinA1-Fc treatment is delivered to the anterior wall to the right of the occlusion, leading to regional differences caused by this treatment. Therefore, being able to analyze strain in more regions would reveal earlier detection of LV dysfunction, and determine specifically where ephrinA1-Fc is affecting the contractile function of the LV.

METHODS

This study was approved by the East Carolina University Institutional Animal Care and Use Committee (IACUC AUP#Q228d) and conforms to the guidelines by the National Institute of Health for the Care and Use of Laboratory Animals. Data was collected in Greenville, NC. The study is a secondary analysis of an existing data set.

Objective

The purpose of this study is to develop a methodology to analyze the strain and strain rate in mice post-MI and treatment at 12 different segments along the myocardium to determine the LV function and effectiveness of the treatment. In the future, this will optimize the treatment process by determining the location being treated and extent of treatment to the infarct and remote regions of the heart. This study has four specific aims that must be successfully achieved.

1. Detect the edges of the epicardium and endocardium to create radial vectors and segments.
2. Implement speckle tracking to determine displacement of the ventricle wall.
3. Calculate the strain and strain rate based on the radial vector created and the tracking of the LV.
4. Validate strain and strain rate results from the proposed image processing algorithm.

Experimental Protocol

Working with data previously collected in Dr. Virag's lab, the experimental protocol was as follows. Animals were housed in 12 h/12 h light/dark cycle conditions and received food and water ad libitum. Wildtype mice (10-14 weeks) were anesthetized with an intraperitoneal injection of 20 μl/g body weight of tribromoethanol (20 mg/ml) and mechanically ventilated

(Dries et al 2011; DuSablon et al. 2017; Virag and Lust 2011). Surgical procedures were performed by Dr. Jitka Virag as follows. The left anterior descending (LAD) coronary artery was temporarily ligated for 30 minutes using an 8-0 suture, following with 24 hours reperfusion (Dries et al. 2011; Virag and Lust 2011). Ischemia was checked by blanching the myocardium distal to the ligation (Dries et al. 2011). Sham controls were performed with the suture pulled through the heart without ligation (Dries et al. 2011). Within 1 minute of coronary ligation, an intramyocardial injection of either 6 μg IgG-Fc (R&D), or 6 μg ephrinA1-Fc (Sigma) (both in 6μl) was given using a Hamilton syringe with a sterile 30 gauge needle (Dries et al. 2011; Virag and Lust 2011). The investigator performing the surgeries was blinded to the treatments (Driest et al. 2011). All animals were monitored every hour for the first 8 hours post-operatively and then four hours preceding echocardiography and euthanasia (DuSablon et al. 2017).

Image Acquisition

Echocardiography was performed with the Vevo 3100 (VisualSonics, Toronto, Canada) diagnostic ultrasound with a 30MHz linear-array transducer used. Echocardiography was performed blindly to surgical procedure and injection. Both motion mode (M-mode) and brightness mode (B-mode) views were acquired by Dr. Jitka Virag, shown below in Figure 8. M-mode was acquired at mid-papillary level. B-mode images are real-time black and white images of the heart to view heart structure and function, where M-mode images are a sequence of B-mode images over time at a single axis or line to visualize the wall's contractile motion (Ram et al. 2011). All acquisitions were performed on conscious, restrained mice in supine position at 24 hours post-MI. Standard parasternal long-axis and short-axis 2D gray-scale echocardiographic images were obtained. Images were acquired at a frame rate of >300 frames/second. Echocardiographic imaging measurements were performed offline. Mice were then anesthetized

with lethal intraperitoneal injection of 0.1 mL pentobarbital (390mg/ml) (Virag and Lust 2011; DuSablon et al. 2017).

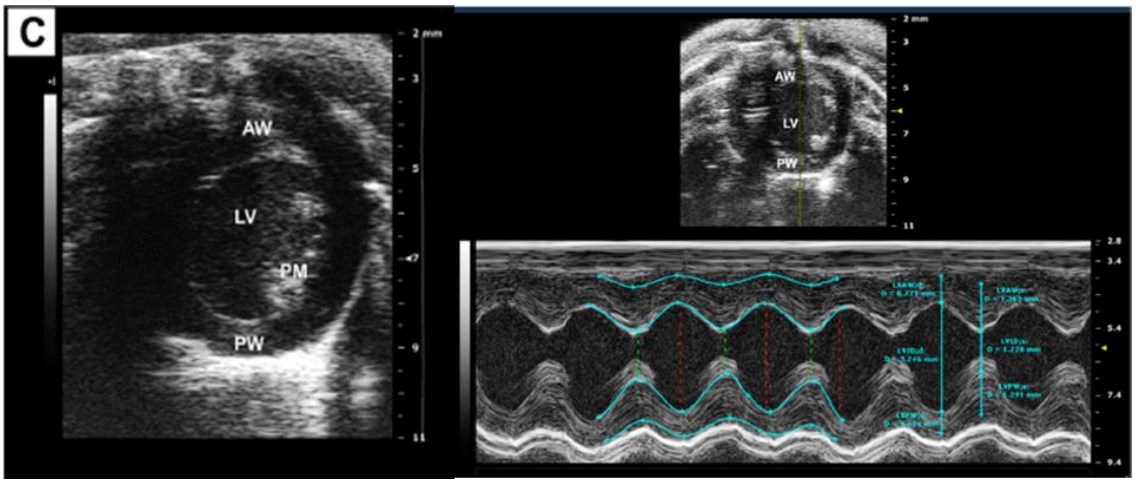

Figure 8 B-mode (left) and M-mode (right) Image Views of Murine Heart (Ram et al. 2011)

Image Processing

Figure 9 represents the steps performed to process the echocardiographic images.

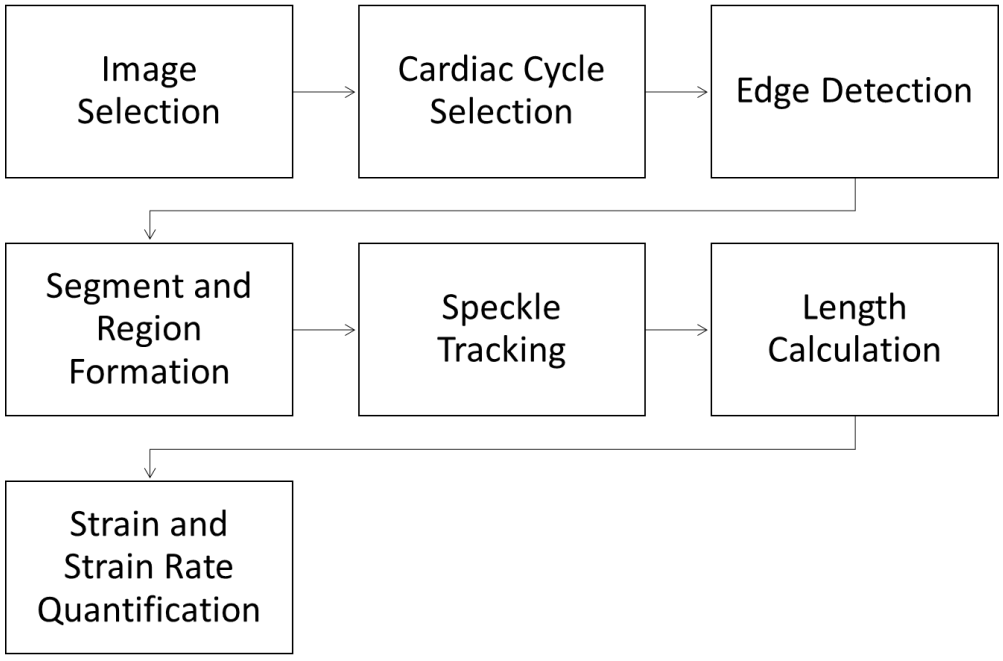

Figure 9 Block Diagram of Image Processing

First, the imaging sets were selected based on clearly defined criteria. From the imaging set, three consecutive cardiac cycles were selected. The contours of the epicardium and endocardium

of the LV were detected, and radial vectors were generated between these surfaces. The LV was then divided into 12 segments with regions aligned with the radial vector at the epicardium and endocardium. The speckle tracking was then performed to determine the displacement of the LV throughout the defined cardiac cycles. The length between the epicardium and endocardium was measured and manually verified to ensure the proposed algorithm was accurately tracking the wall motion. Finally, strain and strain rate were calculated. The processing steps are explained in greater detail below.

Image Selection

The echocardiograms were analyzed offline using MATLAB. Echocardiographic images obtained in Digital Imaging and Communications in Medicine (DICOM) format were uploaded into MATLAB. The best quality long axis cine-loop B-mode images were visually selected for analysis. Three mice per experimental group were selected. The experimental groups were sham (S), which represents a healthy mouse, post-MI with intramyocardial injection of IgG-Fc (MI), which represents an injured mouse, and post-MI with intramyocardial injection of ephrinA1-Fc (T), which represents a treated mouse. In order to accurately quantify the LV function, the images must display well-defined epicardial and endocardial borders. Therefore, there cannot be shadowing over these borders from the ribs as this will cause dark spots over these areas. In addition, images with unwanted artefacts due to breathing were avoided because this could affect the strain results. An example of a high-quality image versus an image with shadowing for both long and short axis can be seen below in Figure 10.

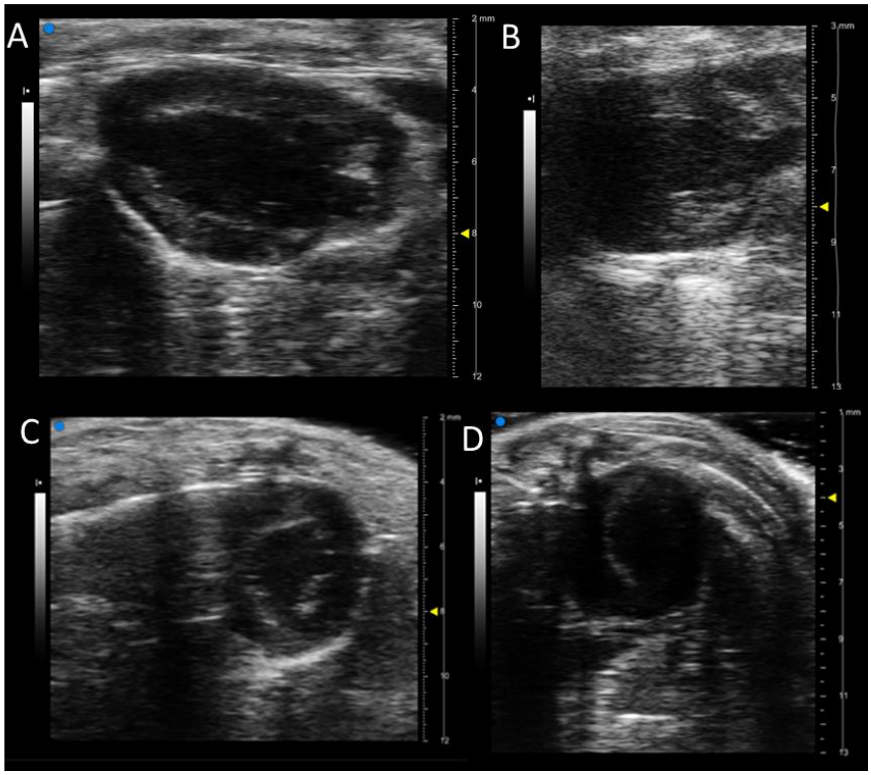

Figure 10 Healthy Mice Heart during Diastole A) long axis, good quality B) long axis, shadowing over apex C) short axis, good quality D) short axis, shadowing over lateral side

To objectively select good quality images, the following criteria were set. For a short axis image, the LV must be circular with a portion of the papillary muscle shown at the intraventricular septum (Buttars 2018; O'Connell 2018; Echocardiography 2018). Two of the papillary muscle must be in view at the 2 and 4 o'clock position (O'Connell 2018). In addition, the RV must be shown, with the LV anterior and posterior endocardium border visible (Buttars 2018; O'Connell 2018; Echocardiography 2018). For a long axis image, the aorta and apex should be on the same horizontal plane, with a clear aortic opening (O'Connell 2018; Echocardiography 2018). The RV outflow tract and apex must be visible (Buttars 2018; O'Connell 2018; Echocardiography 2018). Finally, the LV should have an oval shape. An example of a short axis and long axis image meeting the set criteria can be seen below in Figure 11.

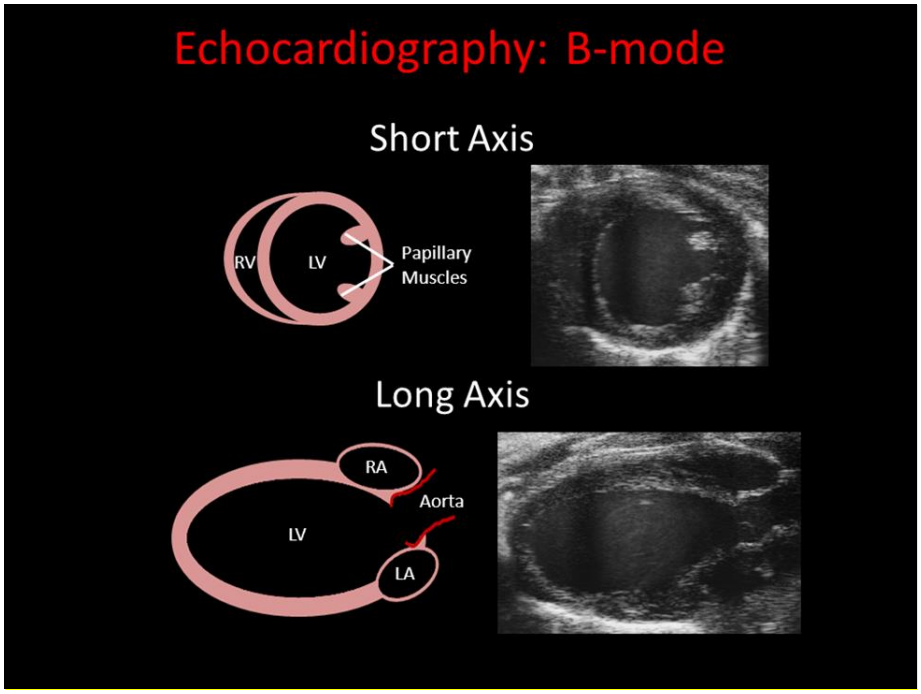

Figure 11 Good Quality Echocardiography Images that meet Selection Criteria (Echocardiography 2018)

Once the cine-loop image was chosen, the cardiac cycles that the speckles were tracked across were selected. In MATLAB, a vertical axis line perpendicular to the LV wall was selected across the center of the chamber. A new matrix was created displaying all the rows with only the selected axis column for each image across time. This created an m-mode image of the LV shown below in Figure 12.

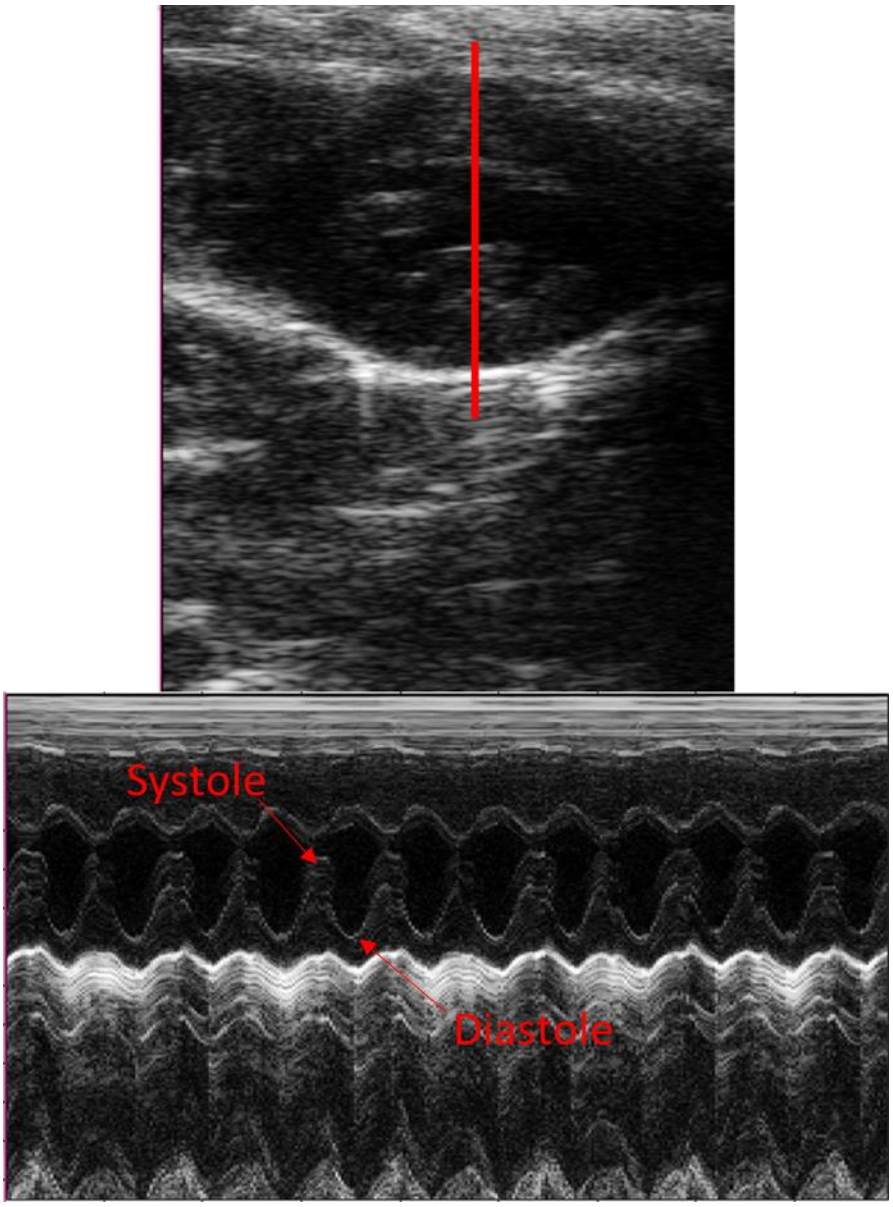

Figure 12 MATLAB Generated M-mode Image

Similar to the current VevoStrain method, three consecutive cardiac cycles were manually selected from the echocardiographic M-mode image. Cycles with unwanted breathing artefacts were excluded. The cycles selected always started and ended at end-systole. The images during the three cardiac cycles selected were the only images from the echocardiogram recording used for the following steps.

Edge Detection

To quantify strain, a region of interest was selected where the motion of the speckles in this area was tracked (Blessberger et al. 2010). The region of interest was the area between the epicardial and endocardial borders of the LV. To trace these contours, the points along these borders were manually selected by clicking along the borders and storing these coordinates in a matrix at the first time point of the selected cardiac cycles. An interpolating cubic spline was then generated and plotted along the epicardium and endocardium, as displayed in Figure 13.

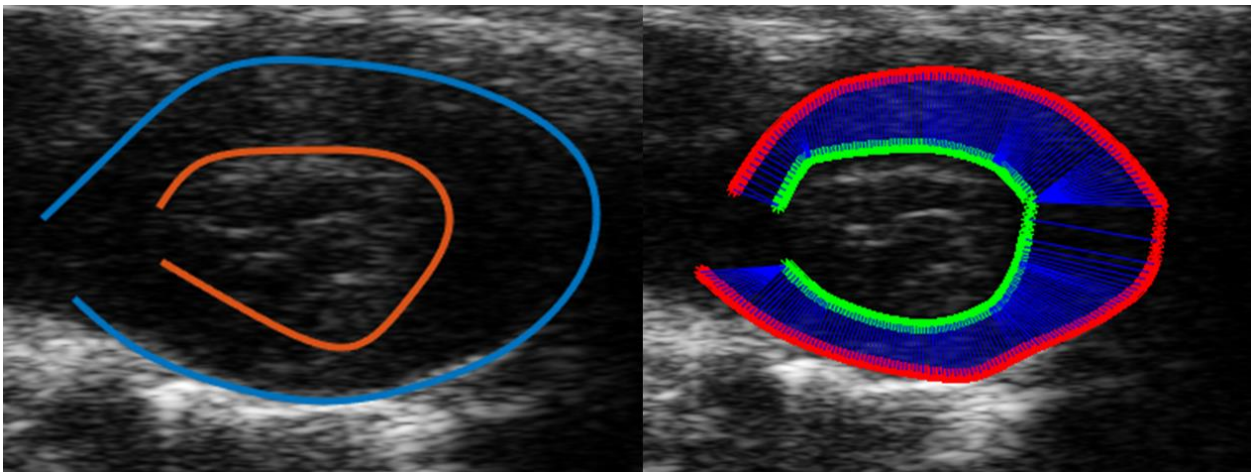

Figure 13 (Left) Epicardial and Endocardial Contour Tracing with Proposed Algorithm for Edge Detection (Right) Interpolated Points along Edges of LV Wall

Interpolation was then performed to increase the number of points selected along these borders from approximately 10-15 points to 600-1200 points, depending on the size of the mouse heart. This is shown above in Figure 13, where green represents the endocardium and red represents the epicardium. From the interpolated points generated along the edges of the epicardial and endocardial borders, radial lines were created by connecting the points on the endocardium to the closest points on the epicardium at the first time point using the distance2curve function in MATLAB. One radial line was selected per segment and designated as the radial vector for the segment, which is used later in the strain analysis. The radial vector was created by selecting a set of those connected points, so the vector is located across the middle of the segment for each

segment. The magnitude of this vector provided the initial length between the epicardium and endocardium.

Speckle Tracking

To track the displacement of the LV wall, the following steps were performed. First, a mask was created to measure the area between the epicardium and endocardium, shown below in Figure 14. The measured area determined by the mask was increased to encompass a larger area around the edges of the epicardium and endocardium, and this larger area was then divided equally into 12 segments for each mouse, as the size of the hearts varied. This was performed at the initial time point, which was end-systole since this is when the thickness between the epicardial and endocardial is greatest. The location of each segment were manually entered by selecting the coordinate of the pixel where the segment begins in the top left corner, and the height and width of each segment. This starting location was manually entered for each segment for each mouse. Segment one started at the anterior base of the LV with segment 12 ending at the posterior base. The orientation of the segment was selected based on the shape of the LV at that location so that the area of the LV wall was covered. These segment locations were selected with the aid of a video feature in MATLAB to ensure the selected segment location covered the endocardium and epicardium contours as best as possible. As shown earlier in Figure 5, the VevoStrain software divides the region of interest into the 6 anatomical segments.

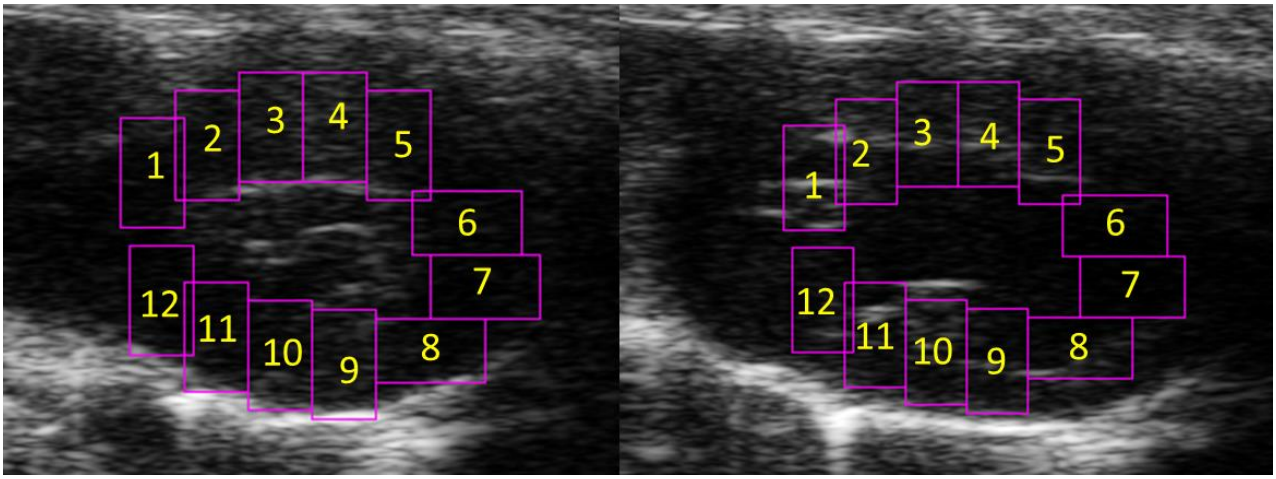

Figure 14 Newly Defined Regions of the LV with Axis Orientation (Left = Systole, Right = Diastole)

Using a point tracking method, a set of points in the region of interest was tracked, using the Kanade-Lucas-Tomasi (KLT) feature-tracking algorithm for the selected cardiac cycles. Points containing the same speckle pattern in the defined search area were tracked frame-by-frame, shown below in Figure 15, reacquiring new points between each time frame as points are easily lost due to the high amount of noise in the echocardiographic images. This process is different compared to the VevoStrain software which acquires speckles at the beginning of the three cardiac cycles and tracks those same speckles every frame.

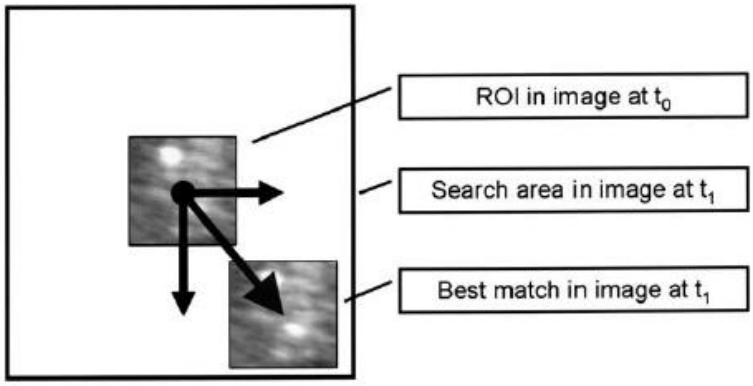

Figure 15 Speckle Tracking Process for Two Consecutive Frames (Amundsen et al. 2006)

Each segment was divided into quadrants. Although points were tracked in all quadrants, the points located in the quadrant closest to the epicardium were used to calculate the epicardial

displacement and points located in the quadrant closest to the endocardium were used for endocardial displacement. The selected quadrants aligned with the radial vector shown as the purple line in Figure 16. The displacement vector between the initial point (red) and new, tracked point (green) was measured for each point for each frame, shown below in Figure 16, where the circles represent the epicardial quadrant and the triangles represent the endocardial quadrant. The median displacement of the points in each quadrant was calculated. The median was used instead of the average displacement to prevent skewing from outliers.

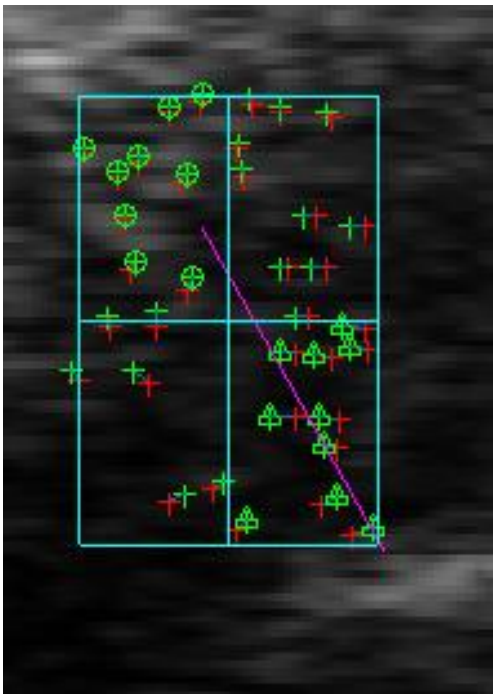

Figure 16 Tracked Points in Epicardial and Endocardial Quarters of Segment 2. Red = initial point, Green = tracked point, Circle = epicardial quadrant, Triangle = endocardial quadrant

The radial unit vector was determined by dividing the vector by the vector magnitude which allowed for the created of a radial axis. The dot product was then performed between the unit radial vector and the median displacement vectors from speckle tracking for the epicardial and endocardial quadrants. The dot product gives the displacement in the radial direction, shown below in Figure 17. Blue represents the radial vector, green represents the epicardial and endocardial displacement, and red represents the epicardial and endocardial displacement in the

radial axis direction after the dot product was performed. To calculate the displacement between the epicardium and endocardium in the radial direction, the wall thickness for time frame 1 (the start of the selected cardiac cycles) was added by the displacement for the endocardial quadrant and subtracted by the displacement for the epicardial quadrant, shown below in Equation 3.

$$L(t) = L(t-1) + Disp_{epi}(t) - Disp_{endo}(t) \quad (3)$$

$Disp_{epi}$ represents the displacement from the epicardial quadrant in the radial direction, $Disp_{endo}$ represents the displacement from the endocardial quadrant in the radial direction, and L represents the length between the epicardium and endocardium. The addition and subtraction were based on the orientation of the coordinate system and was performed for segments 1-6. For segments 7-12, the displacement for the epicardial quadrant was added and the displacement for the endocardial quadrant was subtracted. Then for each following time frame, the process was repeated but the previously generated length was used in place of the initial length, represented as L(t-1), to determine how this distance changed with time.

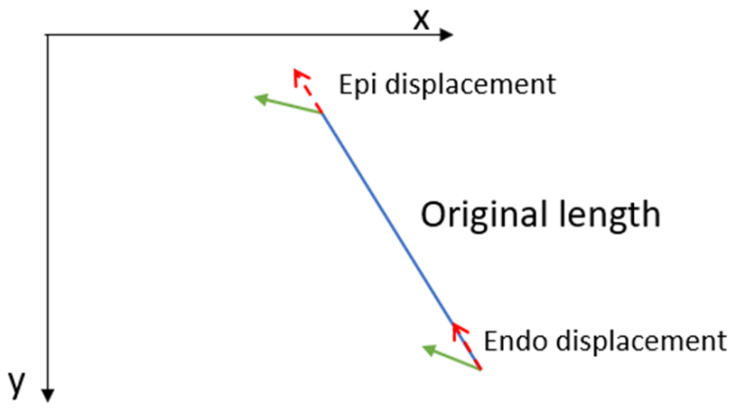

Figure 17 Epicardial to Endocardial length displacement based on radial vector (blue) and displacement vectors (green)

Strain Analysis

To calculate the strain and strain rate based on the speckle tracking results, the following steps were taken. The lengths in the radial direction, calculated with Equation 3, were used to calculate strain with Equation 1, listed earlier. The average diastolic length was used as L_0 for Equation 1. The VevoStrain software uses the length at end diastole (O'Connell 2017). To use a similar length value as the software, the three diastolic time points were determined by looking at the m-mode image, shown above in Figure 12. The length at each diastolic time point, as determined by the proposed algorithm, were averaged and used as the initial length, L_0. Percent strain was calculated each frame and the peak percent strain across the selected cardiac cycles was reported. The strain rate was calculated by dividing the change in strain by the time between each frame, which is provided in the DICOM file.

Validation

To validate the proposed algorithm, the length between the epicardium and endocardium was manually measured. The original radial vector at the initial time point between the epicardium and endocardium was plotted each time frame during the speckle tracking process. The length was manually measured by clicking on the image at the location of the epicardium and endocardium where it lines up with the radial vector. The coordinates of these two points were then used to calculate the magnitude. This is shown below in Figure 18. This was performed on each mouse for at least six time points throughout the selected cardiac cycles to assess whether the proposed algorithm was accurately tracking the displacement of the LV wall. The manually calculated length and the proposed algorithm calculated length were visually compared over the cardiac cycles to assess how well the two methods match.

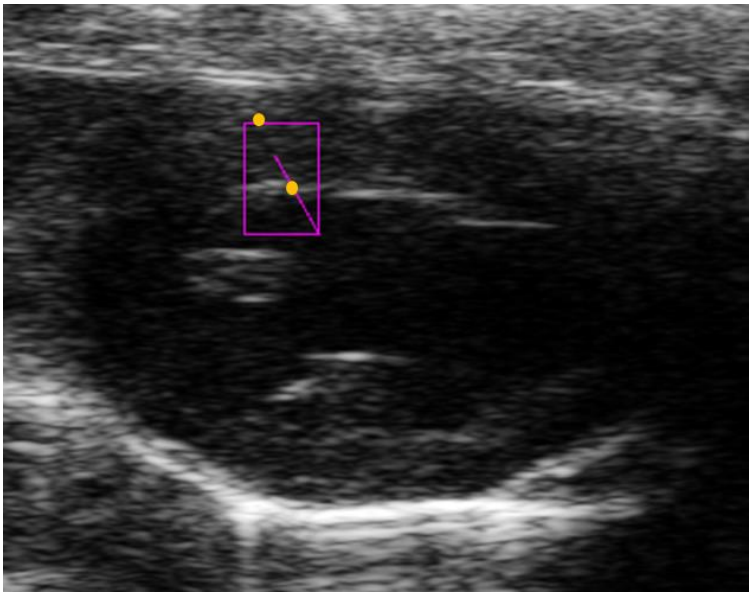

Figure 18 Manual Length Measurement

To further validate the results, the strain analysis was compared to the current speckle-tracking method using the VevoStrain software (VisualSonics). Using the same B-mode images from the novel processing method, the same three consecutive cardiac cycles were selected. The endocardium was manually traced by selecting points along the endocardial border at the starting frame at systole. The epicardium was then automatically traced. An example of the border tracing with this software is shown below in Figure 19. These points were manually adjusted as needed for optimal tracking. Frame-by-frame tracking of these borders was then processed by the software for strain measurements of the LV. The LV was automatically divided into six standard anatomical segments to obtain regional % peak radial strain measurements across the cardiac cycles, shown earlier in Figure 5. Global radial strain values were measured by averaging the 6 segments. To measure LV dyssynchrony, the strain rate peak (1/s) was computed. The percent difference was calculated to compare the global percent peak strain between the two methods for each mouse using the following equation.

$$\%\, difference = \left| \frac{(\varepsilon_{VS} - \varepsilon_{PA})}{\frac{\varepsilon_{VS} - \varepsilon_{PA}}{2}} \right| \times 100\% \quad (4)$$

In Equation 4, ε_{VS} represents the global percent peak strain value from the VevoStrain software and ε_{PA} represents the global percent peak strain value from the proposed algorithm. The percent difference was also determined in the same way comparing the manual length to the proposed algorithm length.

Figure 19 Epicardial and Endocardial Border Tracing

In order to make comparisons between the developed algorithm and the commercial code, the results from the novel method were averaged into six segments. In addition, the global strain values were compared. these strain measurements were averaged across the 12 segments to get global values.

Data Analysis

Once this novel strain analysis was validated, the results from the different animal groups were compared to investigate the significance of ephrinA1-Fc post-MI. The effectiveness of this treatment was analyzed by comparing segmental strain data across the control, MI, and treated groups to see if contractile function improves after administration of ephrinA1-Fc post-MI. This comparison was performed visually by plotting the average strain value for each mouse across time. In addition, the global strain values were ranked from greatest to least to compare the performance between groups.

RESULTS

Nine wildtype mice, both male and female, from 10-14 weeks of age were included for strain analysis. Three female mice were used for the sham group, one female and two male mice were used for the post-MI group, and one female and two male mice were used for the treated group. Using the novel MATLAB algorithm produced in-house, strain was calculated in 12 equal segments along the myocardium.

Validation Analysis

The length between the epicardium and endocardium was calculated across the selected cardiac cycles for each segment through the speckle-tracking algorithm. When plotting the lengths calculated by the proposed algorithm compared to the length measured manually every three frames, the following curves were produced. An example of these curves for sham mouse two is shown below in Figures 20a-c. These figures show the proposed algorithm produced length between the epicardium and endocardium compared to the manual length measured. For the manual curve, only the 35 measured values were plotted (blue circles), which were connected with a curve fitting line. Therefore, the length values between these plotted points, represented by the blue line, are not actual length values.

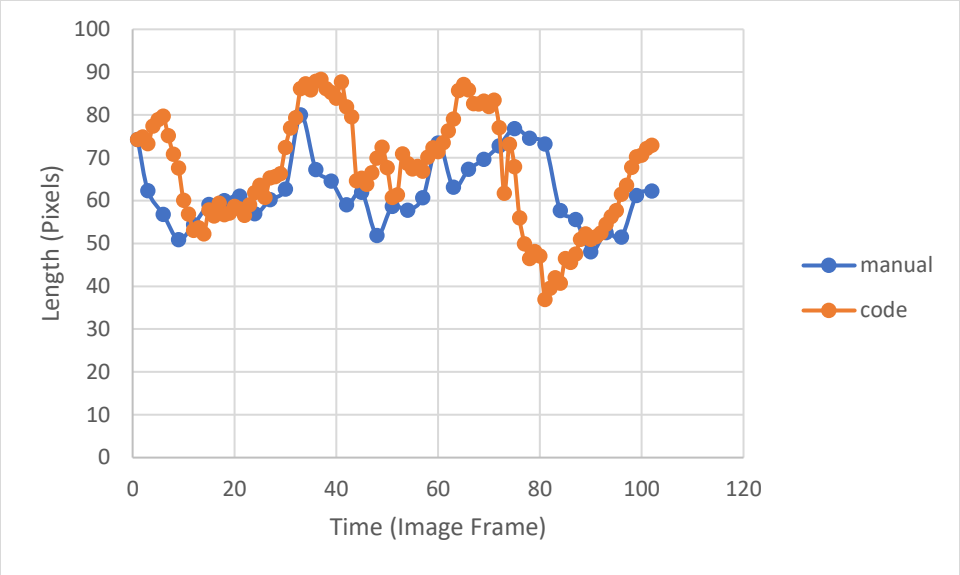

Figure 20a Calculated distance between the Epicardium and Endocardium for Segment 1 of Sham Mouse

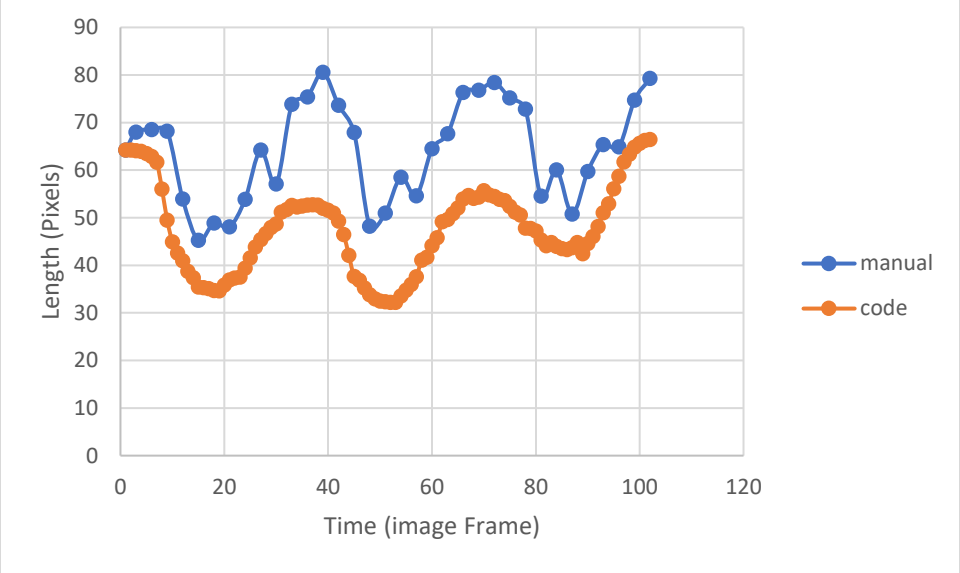

Figure 20b Calculated distance between the Epicardium and Endocardium for Segment 4 of Sham Mouse

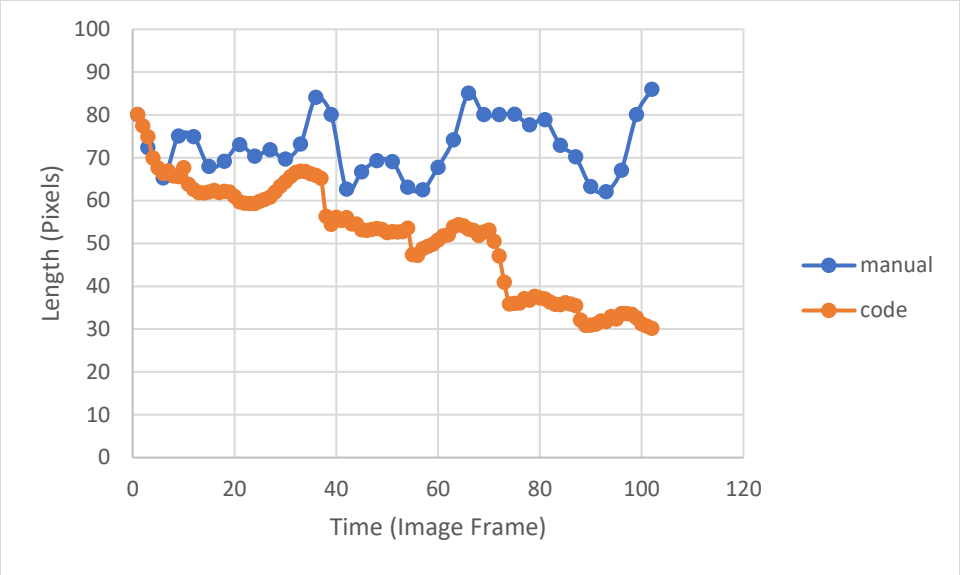

Figure 20c Calculated distance between the Epicardium and Endocardium for Segment 9 of Treated Mouse

These results demonstrate the proposed algorithm's tracking ability varies due to several factors. The majority of the segments produced a length curve similar to Figure 20a, which is an example of the proposed algorithm tracking the contours of the LV somewhat accurately, or Figure 20b, which is an example of the proposed algorithm pretty accurately tracking these contours. This is based on how closely the length values align, in addition to whether the curves are in phase with each other. As you can see in Figure 20a, a large amount of length values are similar however, the curves are out of sync towards the third cardiac cycle showing the proposed algorithm did not track properly at the end. Figure 20b shows the curves in phase, but the length values are different, showing the proposed algorithm is tracking the change in length properly but not the absolute length. Figure 20c is an example of the proposed algorithm poorly tracking the LV wall, as most of the length values are not the same and the curves are out of phase. This was tested for each mouse group in at least two segments per mouse. The length validation results for each mouse are in Appendix A

Data Analysis

The strain and strain rate were calculated for each segment. Figure 21 represents the strain and strain rate measured in segment four of a sham mouse (S2). An average radial strain for long axis, healthy mice is ~50% (O'Connell 2017).

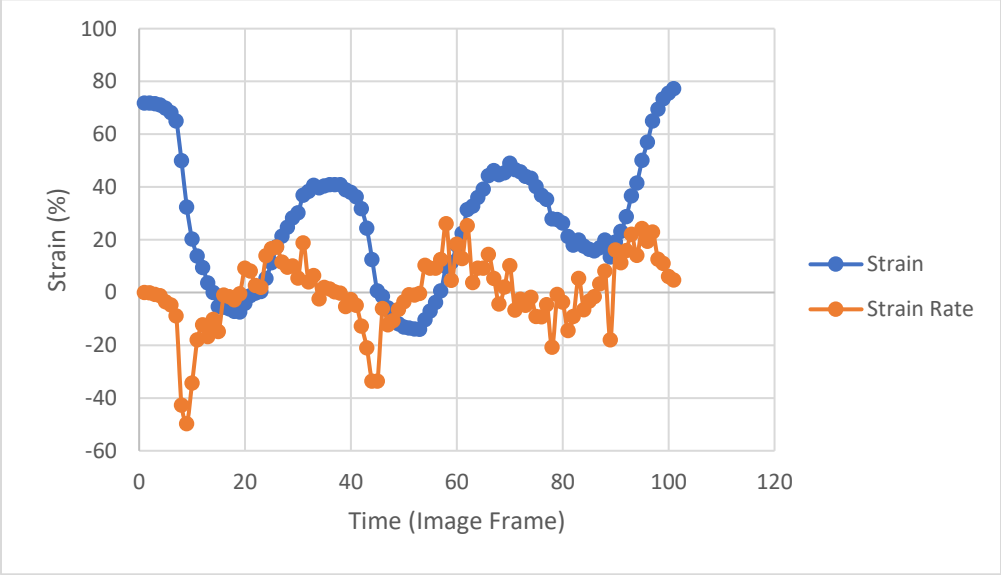

Figure 21 Strain and Strain Rate measured in % Strain and % Strain/seconds

To visually analyze the strain across the different experimental groups, the average strain across all 12 segments was calculated at each time point of the selected cardiac cycles and plotted. This plot is shown in Figure 22a and 22b below. The strain for each mouse was normalized across the three cardiac cycles for comparison. The sham mice followed the pattern of the cardiac cycles shown by the length in Figure 20. The mice treated with ephrinA1-Fc post-MI and the post-MI mice produced a less uniform strain curve with a decreased slope, showing the contractile function has been compromised.

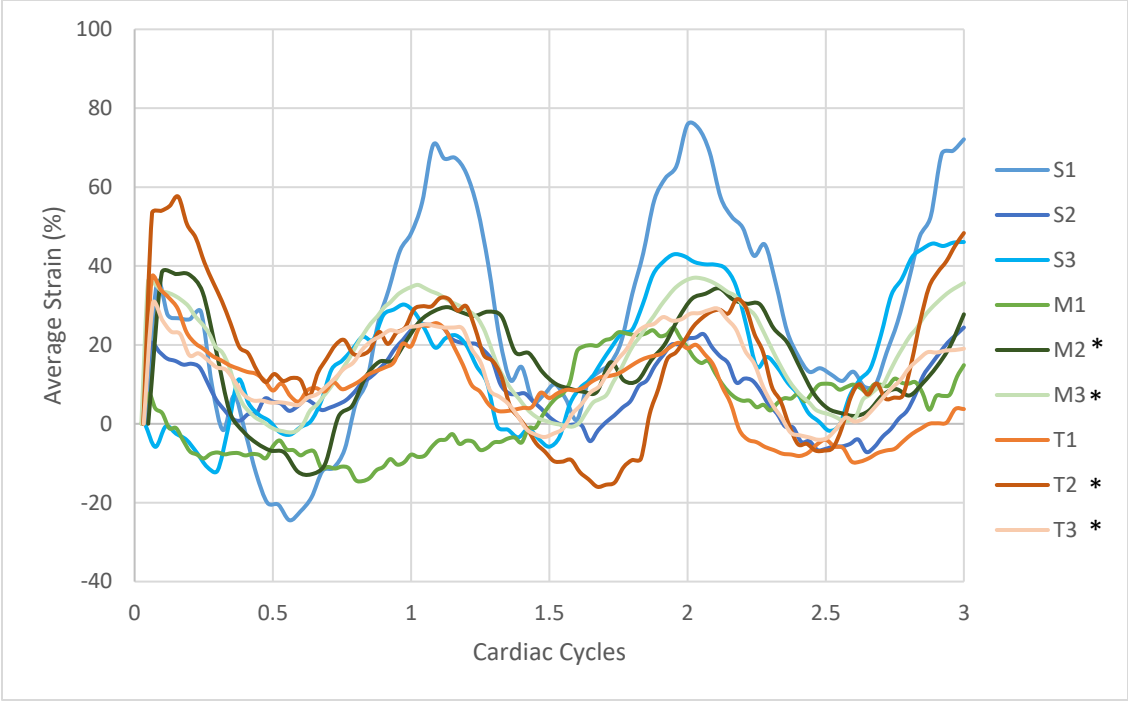

Figure 22a Average % Strain for each mouse across 3 Cardiac Cycles (* = male)

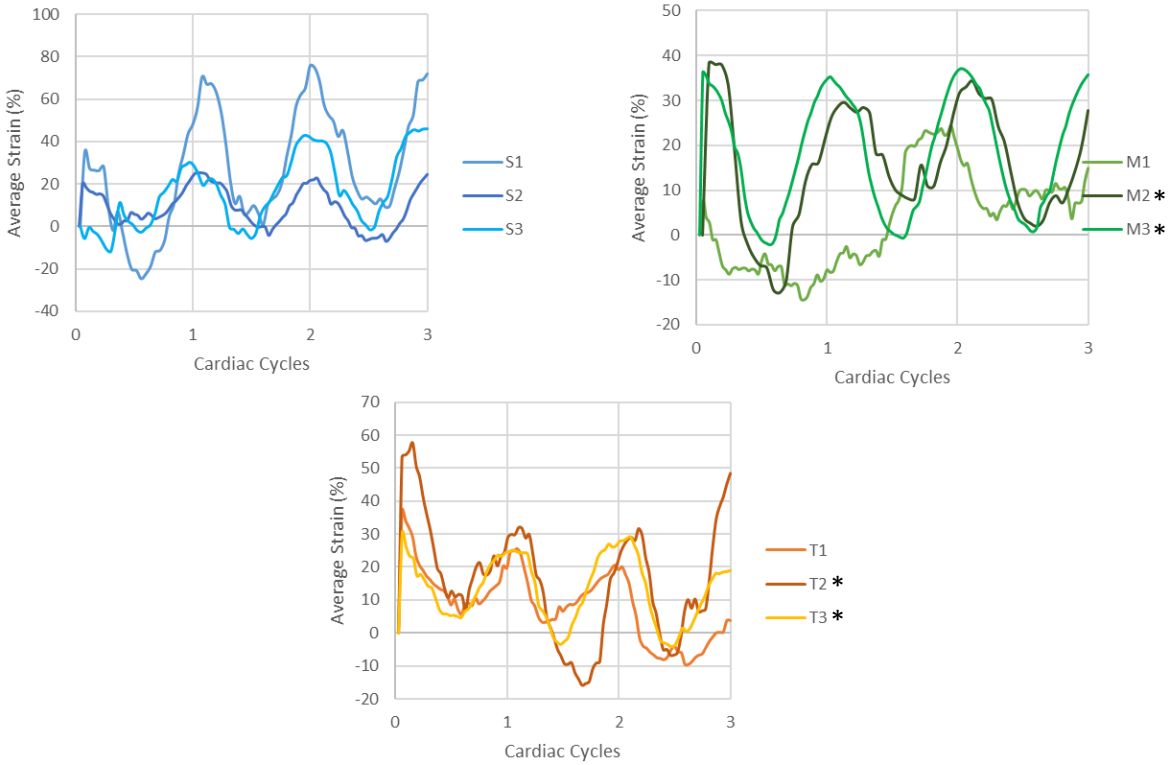

Figure 22b Average % Strain for each mouse per experimental group across 3 cardiac cycles (* = male)

The global strain computed with the proposed algorithm was compared between experimental groups to measure the effectiveness of the treatment. These results, shown below in Table 1 and Figure 23, show the contractile function of the LV was impacted. These are global strain values which means, all 12 segments were averaged. However, as shown earlier, not all segments were accurately tracked, skewing the data. This caused increased global values from inaccurately high strain values for some segments. With that being said, respectively the sham mice had the highest % peak strain values with the treated mice following, and the MI mice being the lowest (average global % peak strain per experimental group was 108.5%, 60.0%, and 51.4%, respectively). It is important to note that this large of strain values, especially in the sham group, has not been reported before in mice. The second mouse post-MI did not follow this trend with a large peak % global strain value due to its rather elevated values along the posterior apex and posterior base segments.

Table 1 Rank of Global % Peak Strain Values (* = male)

Mouse	Global % Peak Strain
S1	193.1
T2*	92.9
S3	78.6
M2*	61.6
S2	53.6
M3*	50.7
T1	47.4
M1	42.0
T3*	39.5

After a coronary ligation, the MI group with the intramyocardial injection of IgG-Fc, referred to as MI in Figure 23, had a lower % peak global strain compared to the sham mice. Overall, the MI+ephrinA1-Fc group, which received the intramyocardial injection of ephrinA1-Fc after coronary ligation, had a higher % peak global strain compared to the MI group based on average % peak global strain values per experimental groups listed earlier. This % strain was less than

the sham group, showing contractile function improves after treatment, but not to the full extent. However, due to a limited data set, no statistical analysis was performed. These trends are what is expected based on previous studies and physiological reasons, but the strain values were greater than expected.

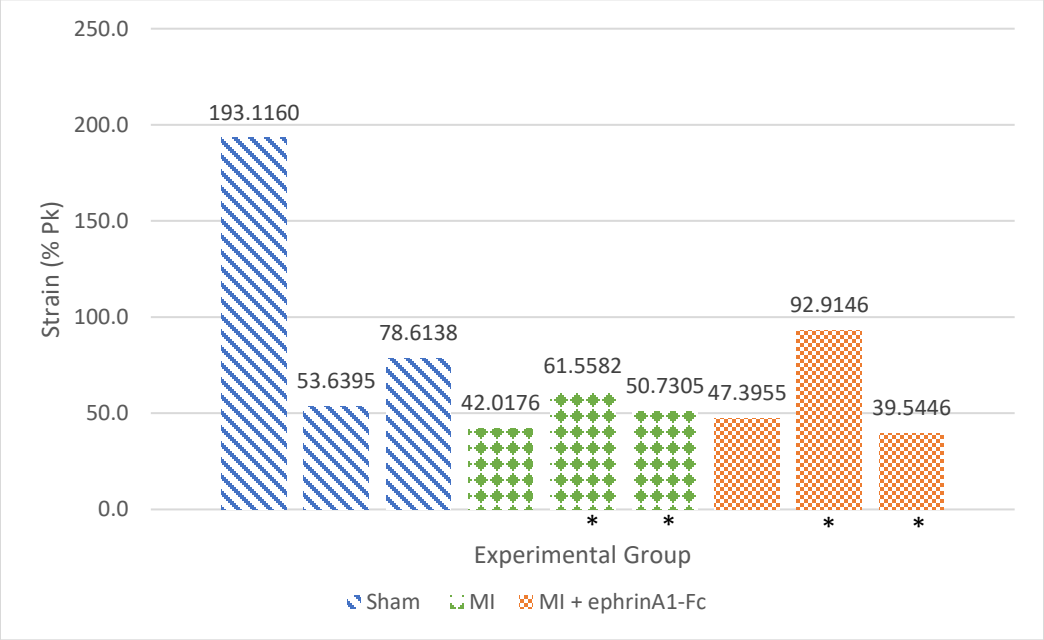

Figure 23 % Peak Global Strain between Experimental Groups (* = male)

The strain values measured with the proposed algorithm were comparable to the expected value of 50% peak strain for a healthy mouse for radial strain in the long axis, with the exception of sham mouse 1 which had unusually high strain values for all segments and was unable to be tracked around the entire apical region due to poor image quality. The global strain rate results are shown below in Figure 24. The strain rate was greatest in the mice with the greatest strain across all experimental groups. The full strain and strain rate results can be found in Table 3 in Appendix B.

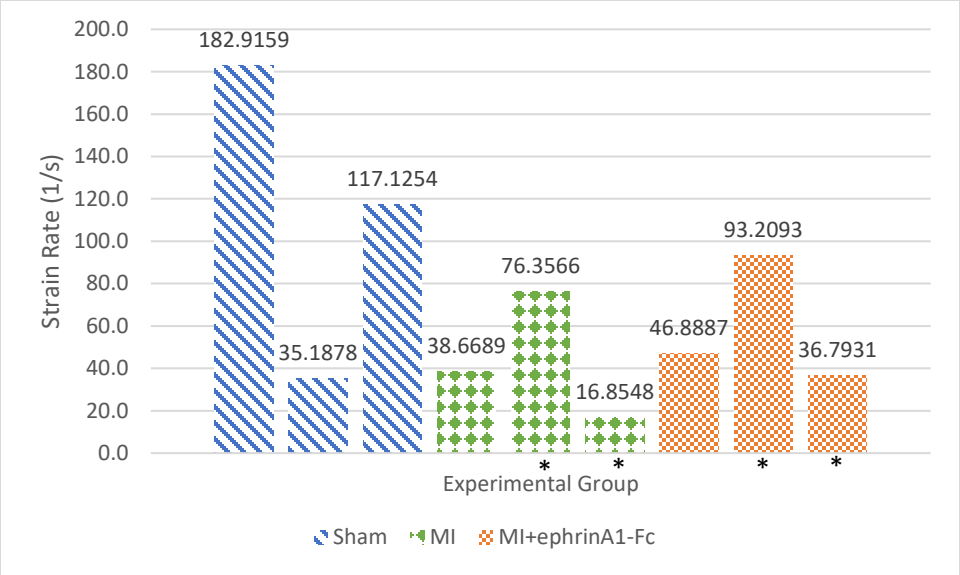

Figure 24 Global Strain Rate between Experimental Groups (* = male)

The global strain values computed with the VevoStrain software were compared across experimental groups to validate the proposed algorithm and commercial algorithm produce similar findings. The proposed algorithm and commercial algorithm % peak global strain values are shown below in Table 2. The percent difference between the two methods was computed using Equation 4 listed earlier.

Table 2 % Global Peak Strain from VevoStrain and Proposed Algorithm (* = male)

Developed Code				VevoStrain				% Difference
Mouse	Global % Peak Strain	Average	SD	Mouse	Global % Peak Strain	Average	SD	
S1	193.1	108.5	74.4	S1	31.5	28.0	3.8	143.9
S2	53.6			S2	28.5			61.2
S3	78.6			S3	24.0			106.4
M1	42.0	51.4	9.8	M1	14.5	19.2	5.3	97.5
M2*	61.6			M2*	18.1			109.2
M3*	50.7			M3*	25.0			68.0
T1	47.4	60.0	28.8	T1	9.8	17.9	11.9	131.2
T2*	92.9			T2*	31.5			98.6
T3*	39.5			T3*	12.4			104.4

These results show the sham mice had the greatest strain values overall. The average % peak strain from the VevoStrain software for the sham, MI and treated groups were 28.0%, 19.2%,

and 17.9% respectively. Excluding the second treated mouse, the post-MI mice actually had greater strain values than the treated mice. This trend is different to what was reported with the proposed algorithm. In addition, the strain values from the VevoStrain software are much smaller compared to the proposed algorithm strain values lowering confidence in the algorithm's values. The global % peak strain values from the VevoStrain software were plotted for each group as well, shown below in Figure 25.

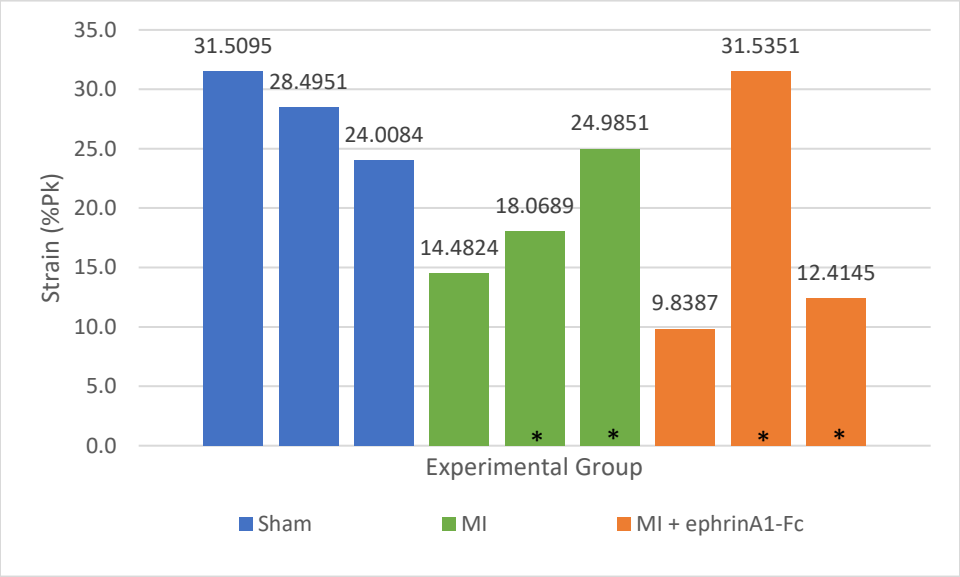

Figure 25 Global % Peak Strain from VevoStrain software (* = male)

The sham mice all had strain values around 30%. The strain was lower in the MI group compared to the sham mice. The average global strain value reported in the treated group was less than the average global strain value for the MI group indicating the treatment may have been ineffective for these mice.

As mentioned earlier, the purpose of this study was to develop a method to compare the strain along 12 segments of the LV. The results across each segment per mouse from the proposed algorithm can be seen below in Figure 26. In the figures, the anterior side of the LV is on the top and the posterior side is on the bottom. The segments that are empty in Figure 26 represent

segments were the proposed algorithm was unable to track the speckles because of shadowing or inability to detect features.

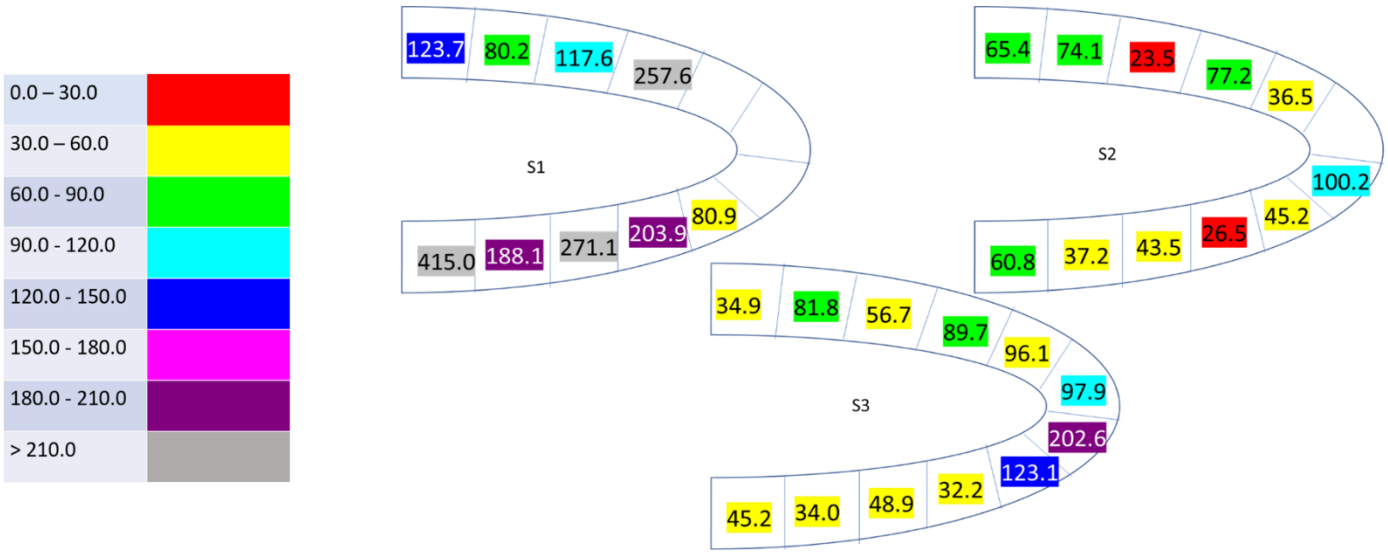

Figure 26a Segmental % Peak Strain for Sham mice

Sham mouse 1 produced extremely high % peak strain values throughout all the segments tracked, shown in Figure 26a. As mentioned earlier, percent peak strain values this large have not been reported before. The high values for sham 1 were consistent for all segments indicating that the tracking of deformation was uniform along the LV wall, but the values recorded were greater than expected. In addition, the proposed algorithm was unable to track along the segments around the apex for this mouse due to shadowing along this area. For sham mouse 2 and 3, the strain was relatively uniform across segments with higher strain values seen around the apex.

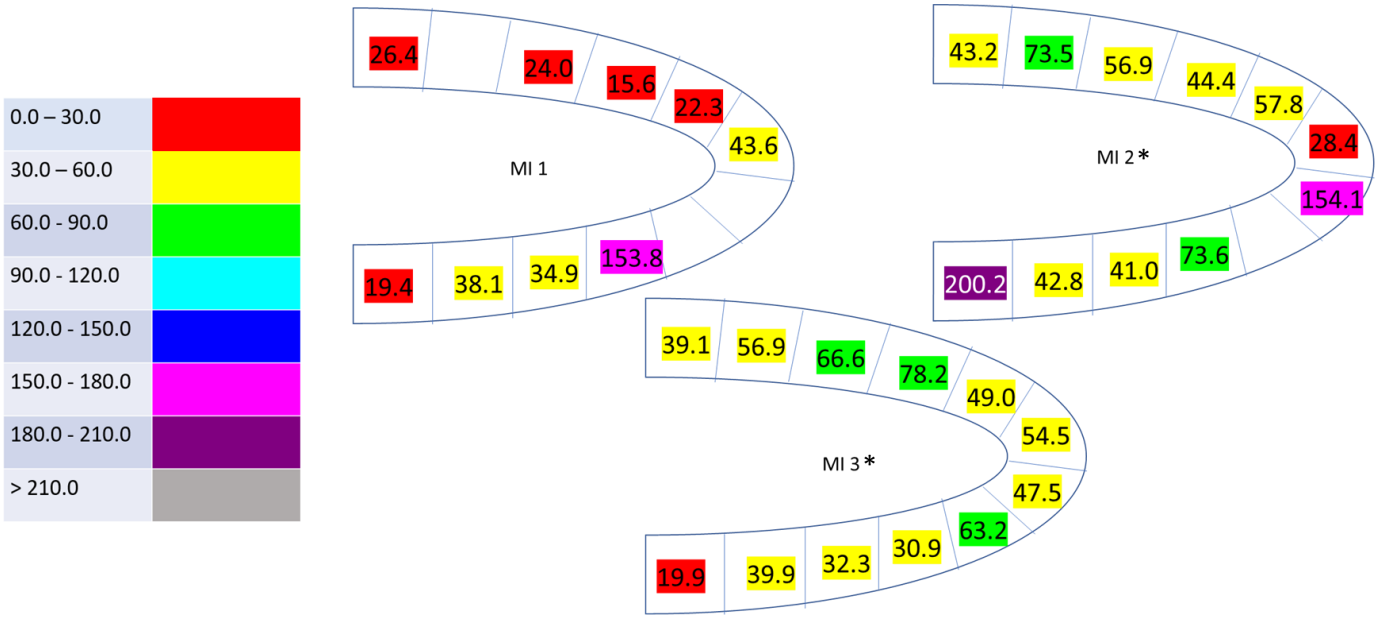

Figure 26b Segmental % Peak Strain for MI mice (* = male)

The strain values were consistent across segments for the post-MI mice, shown in Figure 26b. The first MI mouse reported the smallest strain values. Both MI mouse 1 and 2 resulted in unusually high % peak strain values near the posterior apex at ~150%.

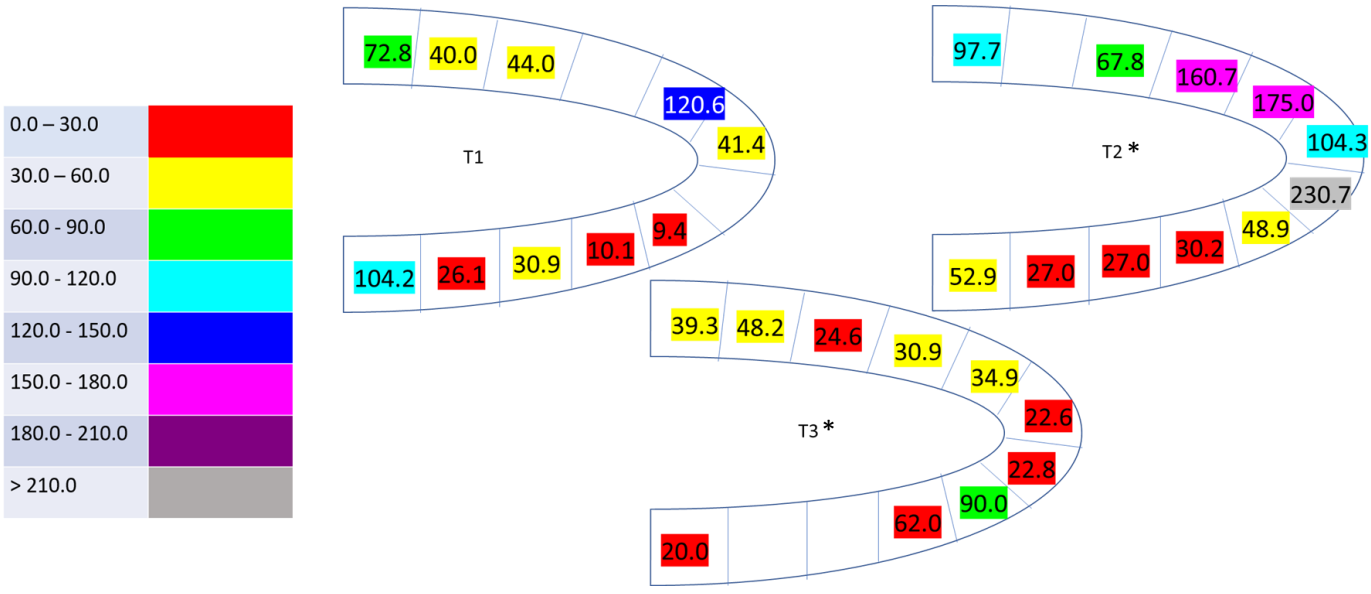

Figure 26c Segmental % Peak Strain for Treated mice (* = male)

As can be seen in the variation in the colors in Figure 26c, the segmental strain values for the mice injected with ephrinA1-Fc post-MI had the greatest range (difference between minimum and maximum strain values) as well as difference between mice. The second treated mouse ranges from 27%-230% peak strain. All three treated mice experience lower strain values along the posterior location of the LV. This suggests the treatment is not reaching this area of the LV wall. To compare segmental strain values from the proposed algorithm across experimental groups, the average percent peak strain for each group and each segment are shown below in Figures 27a-b. The full comparison of segmental strain values across experimental groups is shown below in Appendix C.

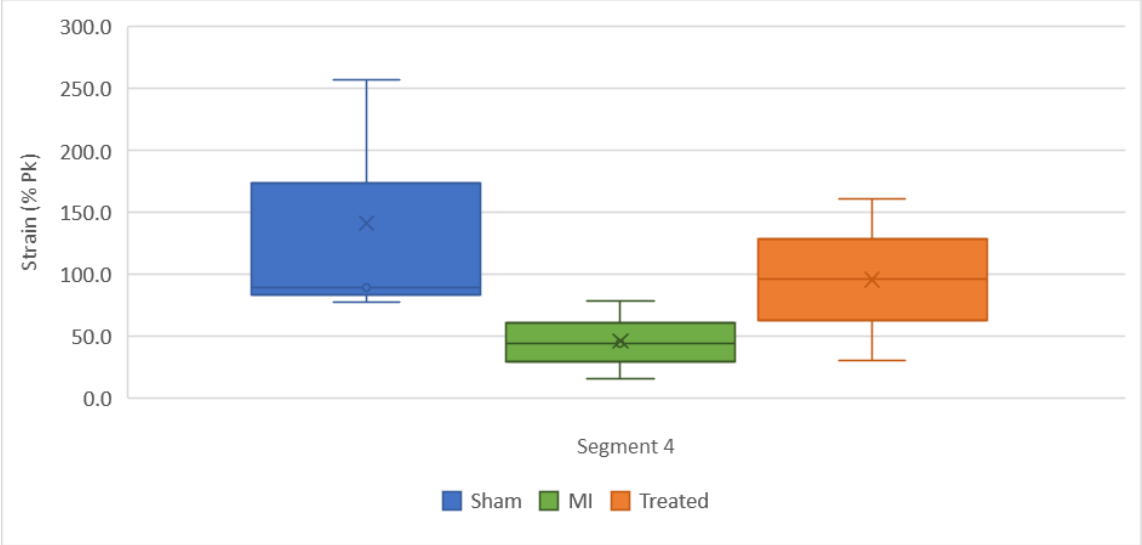

Figure 27a Comparison of % Peak Strain for Segment 4

Figure 27a displays a segment where the results coincide with what is physiologically expected at this segment. The sham group experiences the greatest percent peak strain, with a lower percent peak strain in the post-MI group. The treated group has a higher percent peak strain compared the post-MI group.

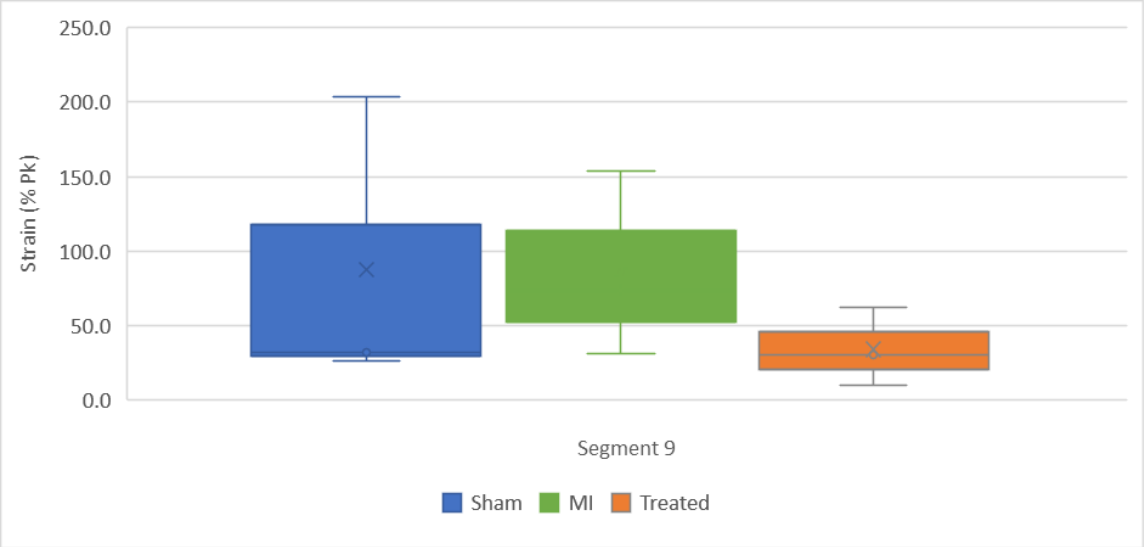

Figure 27b Comparison of % Peak Strain for Segment 9

Figure 27b represents a segment where the data does not physiologically display what is expected. The sham and post-MI group have similar percent peak strain values indicating this location may not be impacted by the occlusion. The treated group resulted in the lowest percent peak strain values, however this is within the healthy range. Also to note for both of these segments, the sham group has the largest interquartile ranges. This may be due to the extremely high values of strain in sham 1.

DISCUSSION

The goal of this project was to develop a proposed algorithm to quantify LV dysfunction through regional strain analysis. This methodology permits measurement of the performance of the LV along 12 smaller segments compared to only 6 segments used with the VevoStrain software, thus enabling more specific, regional measurement of contractile performance in uninjured, infarcted, and ephrinA1-Fc-treated mouse myocardium.

For the proposed algorithm, the sham mice produced the greatest strain, with the treated mice following, and the post-MI mice with the lowest strain values (average global % peak strain 108.5%, 60.0%, and 51.4%, respectively). Apart from the results from the second post-MI mouse and first and third treated mice, the proposed algorithm data follows a physiological expected trend. When the heart is healthy, the contraction is strong, so the heart pumps a greater volume of blood to the aorta. This results in a greater change in radial length when the heart goes from systole to diastole, thus producing a large radial strain value. After an MI occurs, the electrical signal is not conducted across all the myocardium. This produces a decreased contractile force, therefore decreasing the amount of blood pumped to the aorta per heartbeat. With this lower contractile force, the length change between the epicardium and endocardium is less per contraction resulting in a decreased radial strain value. The results from the proposed algorithm do not match the results from the VevoStrain software. The VevoStrain values resulted in the sham producing the greatest strain, with the post-MI mice following, and the treated mice producing the smallest strain values (average global % peak strain 28.0%, 19.2%, and 17.9%, respectively).

When comparing the results from the proposed algorithm and VevoStrain software to strain reported by other groups, the results produce similar trends. Peak percent radial strain values

being greater in the sham group compared to the post-MI group for both the proposed algorithm and commercial algorithm were consistent with similar studies mentioned earlier in the background (Bhan et al. 2014; Bauer et al. 2012; Ram et al. 2011). Ram et al. reported an average radial strain of 43±1.17% for healthy wildtype mice (gender unknown), which was similar to the strain values obtained from the same commercial code, but different for the proposed algorithm. Other studies by Bhan et al. and Bauer et al. compared the strain for healthy and 1 and 7 weeks post-MI mice. These were permanent occlusions and the echocardiograms were recorded when the mice were lightly anesthetized. The mice used for this project were fully conscious and the occlusion was for 30 minutes following with 24 hours reperfusion. With these differences in study parameters noted, the global radial strain values were greater for the sham group (28.0%) compared to the MI group (19.2%) (19.9% sham, 7.5% post-MI, Bauer et al 2012).

For the treatment to be effectively working, the expected strain values would be greater than the post-MI values. The value produced by the proposed algorithm for the 2nd treated mouse was greater than the average strain in the post-MI mice, showing greater contractile function. However, the strain for the first and third treated mice were less than the average strain of the post-MI mice, indicating contractile function was impacted. The mice were different in the post-MI versus treated groups so a direct comparison between mice cannot be done. The radial strain should be smaller around the apical regions of the LV in the post-MI and treated mice compared to the other segments and sham mice as this is downstream the location of the ligation of the LAD. The % peak average strain values were actually greater in this region for the proposed algorithm, while the VevoStrain algorithm showed lower values compared to the other segments.

One factor that may have caused these discrepancies was the gender of the mice. Post-MI and treated mice two and three were males. The rest of the mice were females. The gender of mice could have caused differences in contractile function and effectiveness in the treatment. Overall, the % peak strain was greater in the male mice compared to the female mouse for the post-MI group for both the proposed algorithm and VevoStrain methods. There does not appear to be a gender difference in the reported strain values for the treated mice. However, with a total of nine mice, four of which are male, limited conclusions can be drawn about gender differences.

The values generated from the proposed algorithm were much higher compared to the values reported from the VevoStrain software with an average percent difference of 102.3% between the two methods. These elevated strain values are possibly due to including unwanted artefacts in the speckle tracking process and length calculation, or creating segments based on Cartesian coordinates instead of ellipsoid coordinates, which better aligns with the shape of the LV. In addition, new points are reacquired each time frame unlike the commercial algorithm, which uses the same speckles throughout the entire three cardiac cycles. This may lead to including speckles that represent noise instead of an underlying structure causing these greater strain values. The feasibility of developing a region-specific method to quantify LV dysfunction through strain analysis in mice based on B-mode ultrasound images has been accomplished.

Limitations

There were several limitations faced with the current study. First, a sample size of only three mice per experimental group was selected, preventing a more thorough understanding of the variations between and within experimental groups. However, for the purpose of developing this methodology, three mice per group was sufficient. Also, there can be gender variations between mice which greatly influences baseline size and function as well as response to injury. As for the

size variations, each segment was subject-specific, so this difference was not an issue. Females have been seen to maintain contractile function with the presence of disease due to higher estrogen levels at younger ages (Blenck et al. 2016). The effects of how gender influences treatment of ephrinA1-Fc is still unknown.

In addition to the mice chosen, limitations existed throughout the image processing steps. As shown in Figure 20c, the speckle-tracking algorithm developed does not always accurately track the length between the epicardium to endocardium. For example, in sham 2 segment 12 the average percent difference between manual length and proposed algorithm length was 35.8% with a maximum percent difference of 96.1%. There are several possible reasons for this. If there is shadowing along the LV, the speckles will not be detected. For example, segment 6 is located around the apex where there were often dark shadows for most of the mice, so the contours at the epicardium and endocardium are not well defined. This prevents tracking the speckles at this location, and thus prevents tracking the LV wall deformation. Because there are no values in those segments, the global strain may skewed. These shadows can be seen below in Figure 28. This issue could possibly be addressed by enhancing the image through image processing to make the borders of the epicardium and endocardium visible. However, the speckles may have been lost initially where the ultrasonic beam was unable to reflect light off the LV, so applying a filter to the DICOM image may not result in a more accurate analysis. In addition, some areas along the base of the LV may inaccurately be tracked due to interference from the mitral valve. At times, the speckle-tracking algorithm is detecting the speckles along the valve which creates a length greater than the actual length between the epicardium and endocardium. This was a common problem at segments 1, 2, 10, and 11.

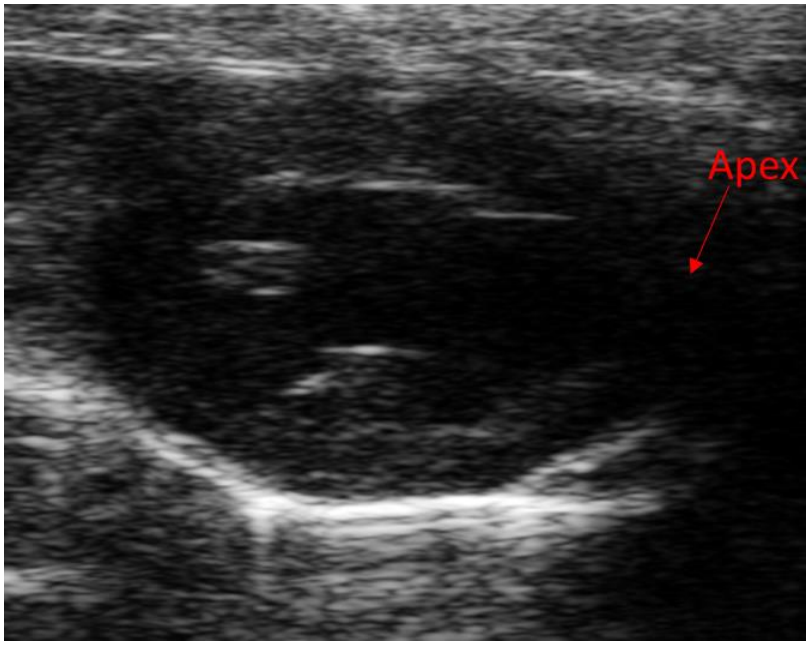

Figure 28 Example of Shadowing at the Apex

In terms of measuring the manual length, the individual performing this task could influence this measurement. The process of manually measuring the length requires looking at the LV at different times along the selected cardiac cycles and clicking points where the initial radial vector lines up at the endocardium and epicardium. If the individual does not accurately select two points at the right location, at the defined contours and in-line with the radial vector, then the manual length will not be a true value. In the future this problem could be addressed by developing a more automatic process to verify the length calculation provided by the proposed algorithm. In addition, the radial vector used to determine the manual length is defined from the initial time frame. However, this line does not move with the pixels, so the epicardium and endocardium points selected at a given time point may not be the same location of the LV wall as originally selected. The LV may shift vertically and/or horizontally throughout the recording of the echocardiography, which is not accounted for in this manual length measurement. This could cause the manual length to be taken from a different location along the LV wall than the original location. This has the possibility of causing issues in validating the speckle tracking algorithm.

There is only one radial vector selected per segment. However, the radial direction is not the same across the entire segment. Therefore, more radial vectors selected per segment could improve the accuracy in tracking the LV wall deformation.

A minor limitation deals with the key step in the strain calculation which is defining the L_0 value used in Equation 1, which represents the unstressed length. As mentioned earlier, the average diastolic length was used as this is how the VevoStrain software defines it. However, this assumes the LV wall is not under any stress at diastole. However, the chamber is full of blood at this point in the cardiac cycle, which applies pressure on the wall. Thus the diastolic length would be smaller than the true, unstressed length, causing a greater strain value.

Another limitation was the three consecutive cardiac cycles selected during the image selection process impact the strain values calculated. Since the echocardiogram images are taken on conscious mice, the mouse's breathing and heart rate may be irregular throughout the recording, as this is a high stress situation for them. When using the MATLAB algorithm developed, the strain values were different for the same segment when different cardiac cycles were selected. Therefore, the same three cycles should be selected for all segments during the image processing stage to get a consistent global strain value. Since the cardiac cycles selected influence the peak % strain results, the same three cardiac cycles should be used for the proposed algorithm and the commercial algorithm during the validation process. A sensitivity study should be performed on the selection of cardiac cycles to better understand the impact of this selection.

It is important to note the differences between the locations of the segments of the proposed algorithm to the VevoStrain software, shown below in Figure 29. The twelve segments determined by the proposed algorithm do not line up exactly with the six segments from the

commercial algorithm. However, when every two segments from the proposed algorithm are compared to commercial algorithm segments, there is a reasonable similarity of areas covered and locations. Therefore, taking the average % peak strain value measured by the MATLAB algorithm for every two segments (1 and 2, 3 and 4, etc.) produces comparable segment locations. These average % peak strain values for every two segments from the proposed algorithm are shown in Appendix B.

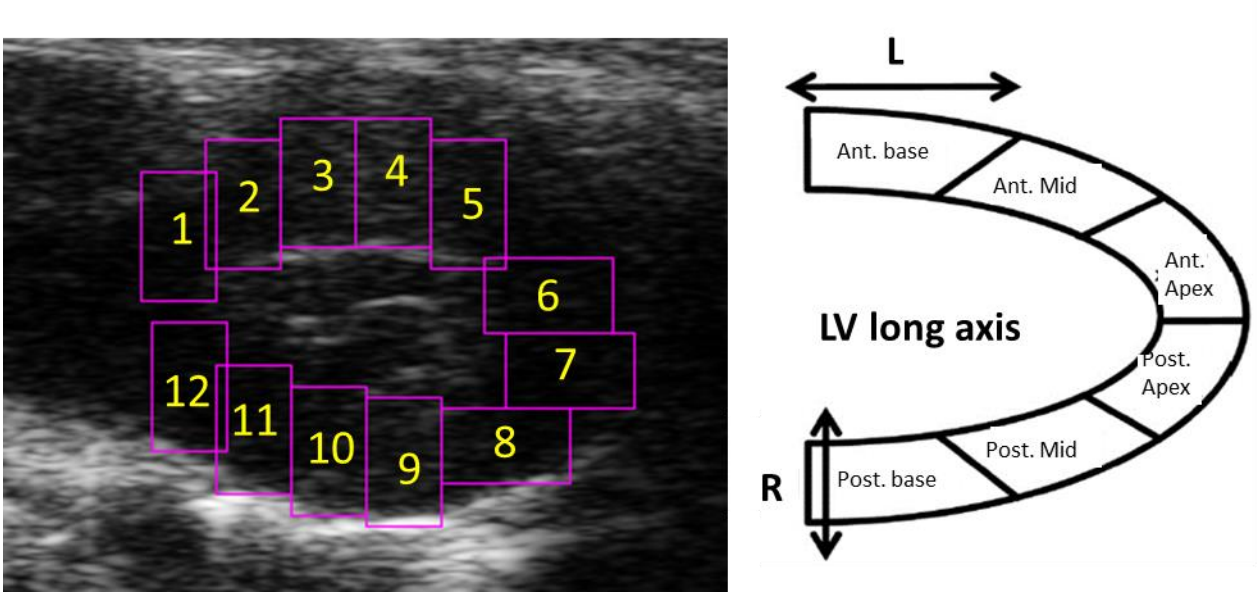

Figure 29 Segment Locations between Proposed Algorithm (left) and Commercial Algorithm (right)

Second, the shape of the segments in the proposed algorithm is different than the shape of the segments in the commercial algorithm. The shape of the segments and the quadrants for selecting the median displacement for the epicardium and endocardium used in the proposed algorithm are rectangular, but the shape of the LV is ellipsoidal. This causes some portions along the epicardium and endocardium to be excluded in the speckle tracking process, in addition to tracking unwanted areas of the echocardiogram. These segments in the proposed algorithm are stagnant where they do not move with the movement of LV wall. This can also cause portions of

the epicardium and endocardium to be excluded in the speckle tracking process at certain time points in the three cardiac cycles.

A key value to having an increased number of segments allows the user to locate specifically where along the LV the heart's contractility is compromised. With the VevoStrain software, the entire anterior apex could be represented as experiencing dysfunction. However, with the MATLAB algorithm, the user may see the location of dysfunction is greater at segment six compared to segment five. This could be extremely useful when administering and analyzing the effects of the ephrinA1-Fc treatment. Unfortunately, the apical region of the LV is where the shadowing and inaccurate tracking occurred most often, making it difficult to evaluate the LV dysfunction at this vital area.

Future Work

As mentioned earlier, feasibility of this method has been shown, but more work is needed to make this tool useful. There are several steps that can be taken to improve the proposed algorithm developed. These steps are as follows:

1. Segment definition

   Adjusting the segments so they align with the VevoStrain software would produce more comparable strain results. Currently, the segments were created based on Cartesian coordinates. Segments should be defined based on the ventricle wall which may be accomplished by using ellipsoid coordinates and the radial vectors. By plotting the segments with ellipsoid coordinates, the segments will better align with the contours of the epicardium and endocardium, and better align with the VevoStrain segment locations.
2. Regions used for tracking

Currently the quadrants used for tracking may not align with the epicardium and endocardium surface. By aligning the regions with the contours of the epicardium and endocardium, the motion of the speckles in the regions should better correspond with the motion of the LV wall. Again, choosing an ellipsoidal coordinate system instead of Cartesian to define the regions will track the epicardium and endocardium more accurately. This would prevent the influence of the mitral valve and limit unwanted artefacts in the strain values. Also allowing the regions to move with the LV as the heart goes from systole to diastole will ensure that the wall is always within the tracking region.

3. Multiple radial vectors per segment

   Only one radial vector was used per segment. However, this could also be improved by selecting more than one radial vector per segment or choosing all the radial vectors to track the entire LV wall deformation.

4. Repeat validation

   The validation process should be reconstructed by determining a way to more objectively measure the manual length for validation to decrease the bias in the length value. Using the displacements to move the radial vector would include the impact of the LV wall shifting throughout the echocardiography recording in the manual length measurement. This will increase the confidence that the proposed algorithm and manual length are producing similar results, and thus accurately tracking the speckles. After improving the validation process and completing the above three steps, the validation results should be improved.

5. Increase sample size

Increasing the sample size and choosing mice with the same gender will improve the confidence ability for the comparison across experimental groups. Once the sample size is sufficient, comparison across genders should be examined.

6. Obtain circumferential and longitudinal strain

   Currently, only the radial strain and strain rate were measured. Radial strain is the percent change in left ventricular myocardial wall thickness. To get a more thorough understanding of the LV dysfunction, the circumferential and longitudinal strain should also be measured. Circumferential strain will measure the myocardial circumference change, and longitudinal strain will measure the percent change in length of the LV (Ram et al. 2011).

CONCLUSION

The feasibility of analyzing LV dysfunction through region-specific strain analysis using speckle tracking was demonstrated in mice. Once the limitations are overcome and the future work has been completed, this process can be used to measure the performance of the heart. This method will give the ability to assess the contractile function between experimental groups at a more detailed level, due to the increased number of smaller segments. By applying this process, one could locate how the LV is impacted by ephrinA1-Fc and locate the optimal location for more targeted drug delivery.

REFERENCES

Amundsen, B. H., Helle-Valle, T., Edvardsen, T., Torp, H., Crosby, J., Lyseggen, E., Stoylen, A., Ihlen, H., Lima, J.A.C., Smiseth, O.A., & Slørdahl, S. A. (2006). Noninvasive myocardial strain measurement by speckle tracking echocardiography: validation against sonomicrometry and tagged magnetic resonance imaging. *Journal of the American College of Cardiology*, *47*(4), 789-793.

Amundsen, B. H., Crosby, J., Steen, P. A., Torp, H., Slørdahl, S. A., & Støylen, A. (2008). Regional myocardial long-axis strain and strain rate measured by different tissue Doppler and speckle tracking echocardiography methods: a comparison with tagged magnetic resonance imaging. *European Journal of Echocardiography*, *10*(2), 229-237.

An, X., Wang, J., Li, H., Lu, Z., Bai, Y., Xiao, H., Zhang, Y., & Song, Y. (2016). Speckle tracking based strain analysis is sensitive for early detection of pathological cardiac hypertrophy. *PloS one*, *11*(2), e0149155.

Andrews, T. G., Lindsey, M. L., Lange, R. A., & Aune, G. J. (2014). Cardiac assessment in pediatric mice: strain analysis as a diagnostic measurement. *Echocardiography*, *31*(3), 375-384.

Bachner-Hinenzon, N., Ertracht, O., Malka, A., Leitman, M., Vered, Z., Binah, O., & Adam, D. (2012). Layer-specific strain analysis: investigation of regional deformations in a rat model of acute versus chronic myocardial infarction. American Journal of Physiology-Heart and Circulatory Physiology, 303(5), H549-H558.

Bauer, M., Cheng, S., Jain, M., Ngoy, S., Theodoropoulos, C., Trujillo, A., Lin, F.C., & Liao, R. (2011). Echocardiographic Speckle-Tracking–Based Strain Imaging for Rapid Cardiovascular Phenotyping in Mice. *Circulation research*, CIRCRESAHA-110.

Benjamin, E. J., Virani, S. S., Callaway, C. W., Chang, A. R., Cheng, S., Chiuve, S. E., Cushman, M., Delling, F., Deo, R., de Ferranti, S., Ferguson, J., Fornage, M., Gillespie, C., Isasi, C., Jiménez, M., Jordan, L., Judd, S., Lackland, D., Lichtman, J., Lisabeth, L., Liu, S., Longenecker, C., Lutsey, P., Mackey, J., Matchar, D., Matsushita, K., Mussolino, M., Nasir, K., O'Flaherty, M., Palaniappan, L., Pandey, A., Pandey, D., Reeves, M., Ritchey, M., Rodriguez, C., Roth, G., Rosamond, W., Sampson, U., Satou, G., Shah, S., Spartano, N., Tirschwell, D., Tsao, C., Voeks, J., Willey, J., Wilkins, J., Wu, J., Alger, H., Wong, S., & Muntner, P. (2018). Heart disease and stroke Statistics—2018 update: A report from the american heart association. Circulation, 10.1161/CIR.0000000000000558

Benjamin, E. J., Muntner, P., Alonso, A., Bittencourt, M. S., Callaway, C. W., Carson, A.P., Chamberlain, A.M., Chang, A. R., Cheng, S., Das, S.R., Delling, F., Djousse, L., Elkind, M.S.V., Ferguson, J., Fornage, M., Jordan, L., Khan, S., Kissela, B., Knutson, K., Kwan, T., Lackland, D., Lewis, T., Lichtman, J., Longenecker, C., Loop, M., Lutsey, P., Martin, S., Matsushita, K., Moran, A., Mussolino, M., O'Flaherty, M., Pandey, A., Perak, A., Rosamond, W., Roth, Ge., Sampson, U., Satou, G., Schroeder, E., Shah, S., Spartano, N., Stokes, A., Tirschwell, D., Tsao, C., Turakhia, M., VanWagner, L., Wilkins, J., Wong, S., & Virani, S. (2019). Heart disease and stroke statistics-2019 update: A report from the American Heart Association. Circulation, 139(10), e56-e528.

Bhan, A., Sirker, A., Zhang, J., Protti, A., Catibog, N., Driver, W., Botnar, R., Monaghan, M.J., & Shah, A. M. (2014). High-frequency speckle tracking echocardiography in the assessment of left ventricular function and remodeling after murine myocardial infarction. *American Journal of Physiology-Heart and Circulatory Physiology*, *306*(9), H1371-H1383.

Blenck, C. L., Harvey, P. A., Reckelhoff, J. F., & Leinwand, L. A. (2016). The importance of biological sex and estrogen in rodent models of cardiovascular health and disease. *Circulation research*, *118*(8), 1294-1312.

Blessberger, H., & Binder, T. (2010). Two dimensional speckle tracking echocardiography: basic principles. *Heart*, *96*(9), 716-722.

Buttars, S. (2018, November 20). April 2015 Webinar - On Demand Tutorial: How to Measure Cardiac Wall Strain. Retrieved October 4, 2018, from https://www.visualsonics.com/resource/past-webinars/april-2015-webinar-demand-tutorial-how-measure-cardiac-wall-strain

Chan, J., Hanekom, L., Wong, C., Leano, R., Cho, G. Y., & Marwick, T. H. (2006). Differentiation of subendocardial and transmural infarction using two-dimensional strain rate imaging to assess short-axis and long-axis myocardial function. *Journal of the American College of Cardiology*, *48*(10), 2026-2033.

Coronary Heart Disease [Digital image]. (n.d.). Retrieved September 29, 2016, from www.nhlbi.nih.gov

Dries, J. L., Kent, S. D., & Virag, J. A. (2011). Intramyocardial administration of chimeric ephrinA1-Fc promotes tissue salvage following myocardial infarction in mice. *The Journal of physiology*, *589*(7), 1725-1740.

DuSablon, A., Parks, J., Estes, H., Chase, R., Vlahos, E., Sharma, U., Wert, D., & Virag, J. (2017). EphrinA1-Fc attenuates myocardial ischemia/reperfusion injury in mice. *PloS one*, *12*(12), e0189307.

Echocardiography: B-mode [Digital image]. (n.d.). Retrieved October 4, 2018, from https://phenocore.ahsc.arizona.edu/sites/default/files/echo-b-mode-2.gif

Epstein, F. H., Yang, Z., Gilson, W. D., Berr, S. S., Kramer, C. M., & French, B. A. (2002). MR tagging early after myocardial infarction in mice demonstrates contractile dysfunction in adjacent and remote regions. *Magnetic resonance in medicine*, *48*(2), 399-403.

Ferferieva, V., Van den Bergh, A., Claus, P., Jasaityte, R., La Gerche, A., Rademakers, F., Herijgers, P., & D'hooge, J. (2012). Assessment of strain and strain rate by two-dimensional speckle tracking in mice: comparison with tissue Doppler echocardiography and conductance catheter measurements. *European Heart Journal–Cardiovascular Imaging*, *14*(8), 765-773.

Gerber, B. L., Garot, J., Bluemke, D. A., Wu, K. C., & Lima, J. A. (2002). Accuracy of contrast-enhanced magnetic resonance imaging in predicting improvement of regional myocardial function in patients after acute myocardial infarction. *Circulation*, *106*(9), 1083-1089.

Gerczuk, P. Z., & Kloner, R. A. (2012). An update on cardioprotection: a review of the latest adjunctive therapies to limit myocardial infarction size in clinical trials. *Journal of the American College of Cardiology*, *59*(11), 969-978.

Gilson, W. D., Yang, Z., French, B. A., & Epstein, F. H. (2004). Complementary displacement-encoded MRI for contrast-enhanced infarct detection and quantification of myocardial function in mice. *Magnetic Resonance in Medicine*, *51*(4), 744-752.

Gilson, W. D., Yang, Z., French, B. A., & Epstein, F. H. (2005). Measurement of myocardial mechanics in mice before and after infarction using multislice displacement-encoded MRI with 3D motion encoding. *American Journal of Physiology-Heart and Circulatory Physiology*, *288*(3), H1491-H1497.

Gorcsan, J., & Tanaka, H. (2011). Echocardiographic assessment of myocardial strain. *Journal of the American College of Cardiology*, *58*(14), 1401-1413.

Healthwise Staff (2017, April 3). Heart and Coronary Arteries [Digital Image]. Retrieved from https://myhealth.alberta.ca/Health/pages/conditions.aspx?hwid=tp13648

Heusch, G., & Gersh, B. J. (2016). The pathophysiology of acute myocardial infarction and strategies of protection beyond reperfusion: a continual challenge. European heart journal, 38(11), 774-784.

Klabunde, R. E. (2012). *Cardiovascular Physiology Concepts*. Philadelphia, PA: Lippincott Williams & Wilkins/Wolters Kluwer.

Kim, J., Rodriguez-Diego, S., Srinivasan, A., Brown, R. M., Pollie, M. P., Di Franco, A., Goldburg, S., Siden, J., Ratcliffe, M., Levine, R., Devereux, R. B., & Weinsaft, J. (2017). Echocardiography-quantified myocardial strain—a marker of global and regional infarct size that stratifies likelihood of left ventricular thrombus. *Echocardiography*, *34*(11), 1623-1632.

Li, Y., Garson, C. D., Xu, Y., Beyers, R. J., Epstein, F. H., French, B. A., & Hossack, J. A. (2007). Quantification and MRI validation of regional contractile dysfunction in mice post myocardial infarction using high resolution ultrasound. *Ultrasound in Medicine and Biology*, *33*(6), 894-904.

Lindsey, M. L., Kassiri, Z., Virag, J. A. I., de Castro Bras, L. E., & Scherrer-Crosbie, M. (2018). Guidelines for Measuring Cardiac Physiology in Mice. *American Journal of Physiology-Heart and Circulatory Physiology*.

Nakatani, S., Stugaard, M., Hanatani, A., Katsuki, K., Kanzaki, H., Yamagishi, M., Kitakaze, M., & Miyatake, K. (2003). Quantitative assessment of short axis wall motion using myocardial strain rate imaging. *Echocardiography*, *20*(2), 145-149.

O'Connell, K. (n.d.). Basic Cardio Imaging. Retrieved October 4, 2018, from https://visualsonics.litmos.com/course/1362733?r=False&ts=636742443008489799

O'Connell, K. (2017, October 31). Retrieved March 15, 2019, from https://www.youtube.com/watch?v=qdr9Z0itTdo

O'Neal, W. T., Griffin, W. F., Dries-Devlin, J. L., Kent, S. D., Chen, J., Willis, M. S., & Virag, J. A. (2013). Ephrin–Eph signaling as a potential therapeutic target for the treatment of myocardial infarction. *Medical hypotheses*, *80*(6), 738-744.

Ram, R., Mickelsen, D. M., Theodoropoulos, C., & Blaxall, B. C. (2011). New approaches in small animal echocardiography: imaging the sounds of silence. *American Journal of Physiology-Heart and Circulatory Physiology*, *301*(5), H1765-H1780.

Rea, D., Coppola, C., Barbieri, A., Monti, M. G., Misso, G., Palma, G., Bimonte, S., Zarone, M.R., Luciano, A., Liccardo, D., Maiolino, P., Cittadini, A., Ciliberto, G., Maurea, N., & Arra, C. (2016). Strain analysis in the assessment of a mouse model of cardiotoxicity due to chemotherapy: sample for preclinical research. *in vivo*, *30*(3), 279-290.

Roger, V. L. (2007). Epidemiology of myocardial infarction. *Medical Clinics*, *91*(4), 537-552.

Spurney, C., Yu, Q., & Nagaraju, K. (2011). Speckle tracking analysis of the left ventricular anterior wall shows significantly decreased relative radial strain patterns in dystrophin deficient mice after 9 months of age. *PLoS currents*, *3*.

Stefani, L., Toncelli, L., Gianassi, M., Manetti, P., Di Tante, V., Vono, M. R. C., Moretti, A., Cappelli, B., Pedrizzetti, G., & Galanti, G. (2007). Two-dimensional tracking and TDI

are consistent methods for evaluating myocardial longitudinal peak strain in left and right ventricle basal segments in athletes. *Cardiovascular ultrasound*, *5*(1), 7.

Täng, M. S., Redfors, B., Shao, Y., & Omerovic, E. (2012). Velocity Vector Imaging Fails to Quantify Regional Myocardial Dysfunction in a Mouse Model of Isoprenaline-Induced Cardiotoxicity. Echocardiography, 29(7), 818-826.

Texas Heart Institute. (2015, July 1). Heart Anatomy [Digital Image]. Retrieved from https://www.texasheart.org/heart-health/heart-information-center/topics/heart-anatomy/

Theodoropoulos, C., & Xu, A. Strain Analysis–An Overview.

Thygesen, K., Alpert, J. S., Jaffe, A. S., Simoons, M. L., Chaitman, B. R., Bax, J., Morrow, D., & White, H. D. (2012). Third universal definition of myocardial infarction. *European heart journal*, *33*(20), 2551-2567.

Torrens, C. (2016, January 14). ECG Changes in Acute and Chronic MI [Digital image]. Retrieved May 21, 2018, from https://www.lifescitrc.org/resource.cfm?submissionID=10554

Virag, J. A., & Lust, R. M. (2011). Coronary artery ligation and intramyocardial injection in a murine model of infarction. *Journal of visualized experiments: JoVE*, (52).

Zhou, R., Pickup, S., Glickson, J. D., Scott, C. H., & Ferrari, V. A. (2003). Assessment of global and regional myocardial function in the mouse using cine and tagged MRI. *Magnetic resonance in medicine*, *49*(4), 760-764.

Zhu, M., Ashraf, M., Zhang, Z., Streiff, C., Shimada, E., Kimura, S., Schaller, T., Song, X., & Sahn, D. J. (2015). Real Time Three-Dimensional Echocardiographic Evaluations of Fetal Left Ventricular Stroke Volume, Mass, and Myocardial Strain: In Vitro and In Vivo Experimental Study. *Echocardiography*, *32*(11), 1697-1706.

APPENDIX A: Length Validation

Sham 1

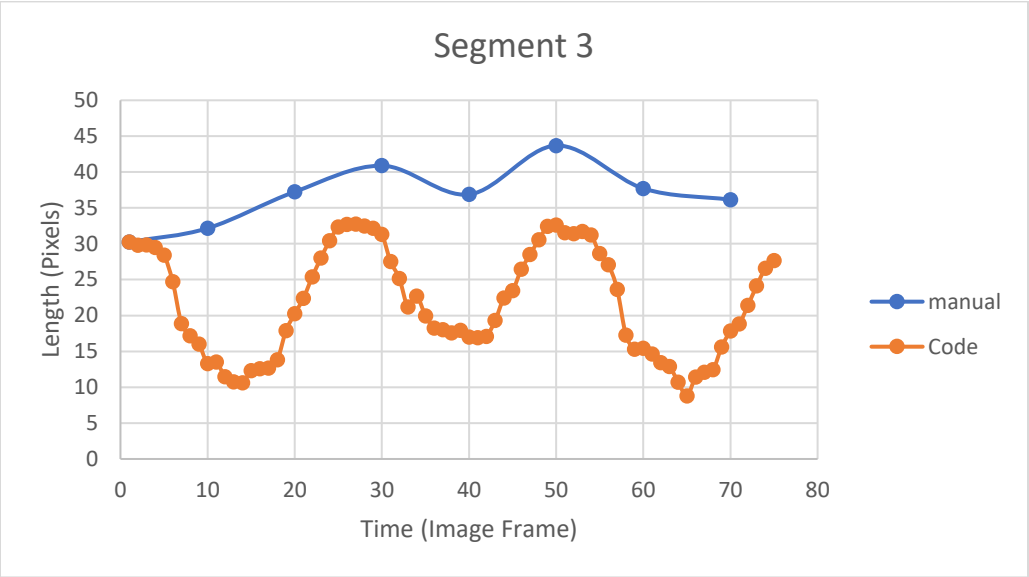

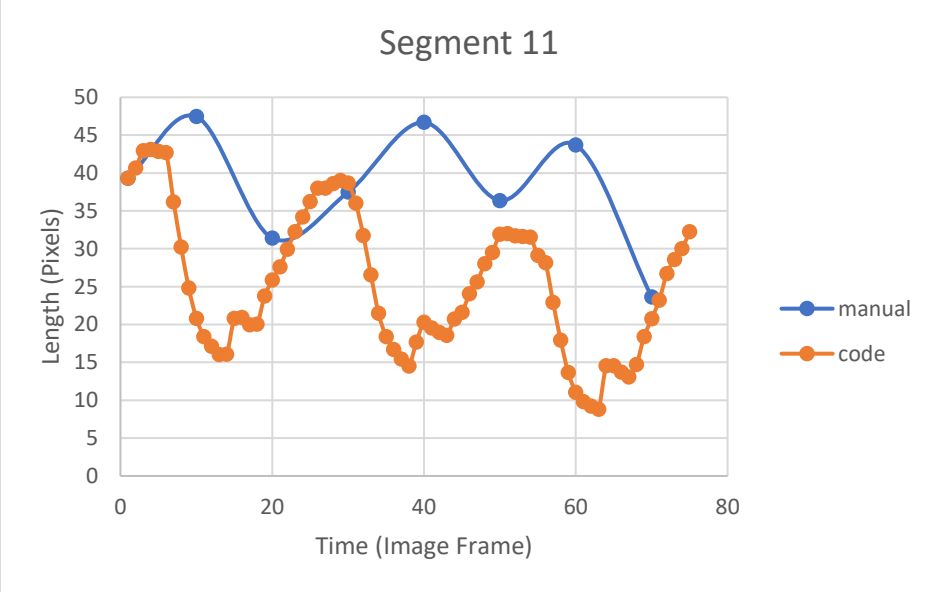

Sham 2

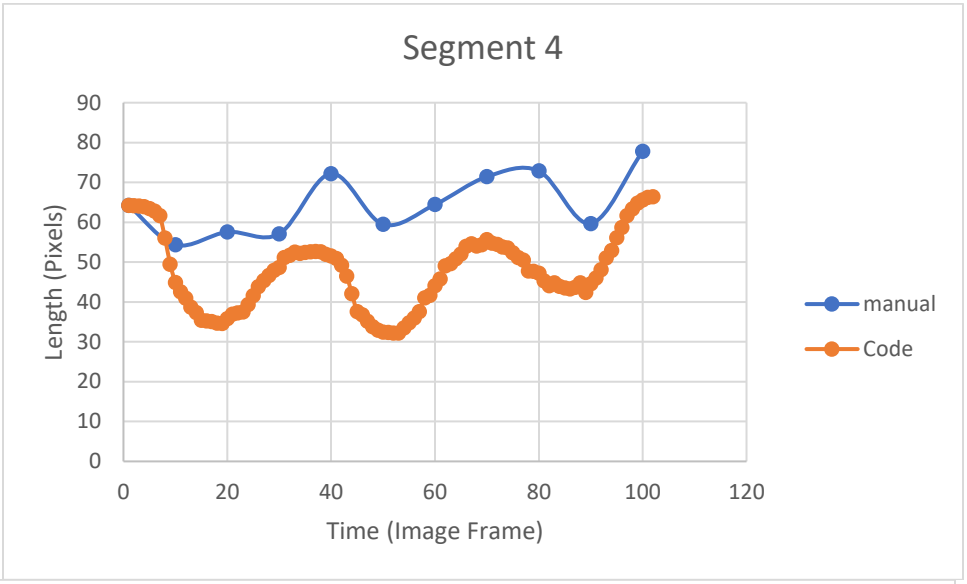
Segment 4
Length (Pixels)
Time (Image Frame)
manual
Code

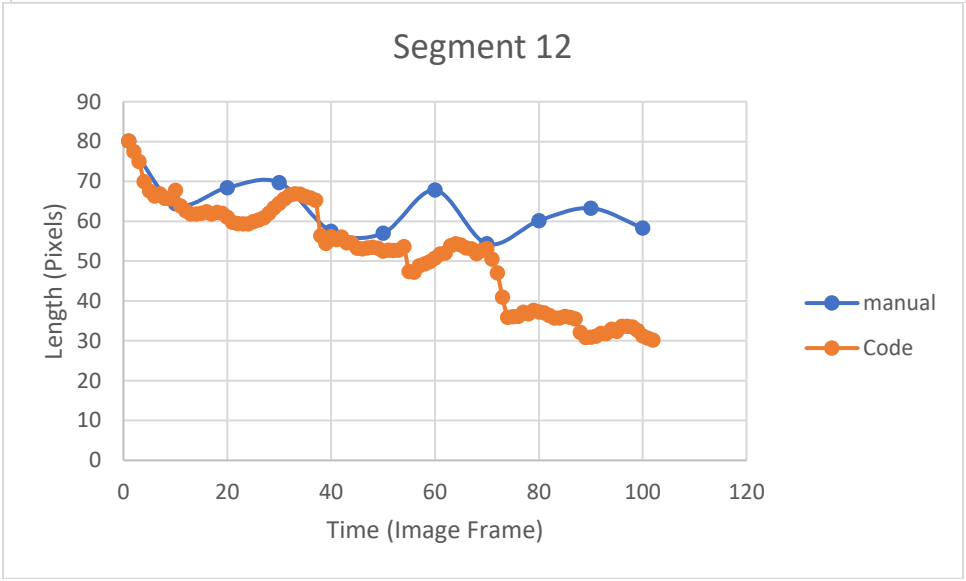
Segment 12
Length (Pixels)
Time (Image Frame)
manual
Code

Sham 3

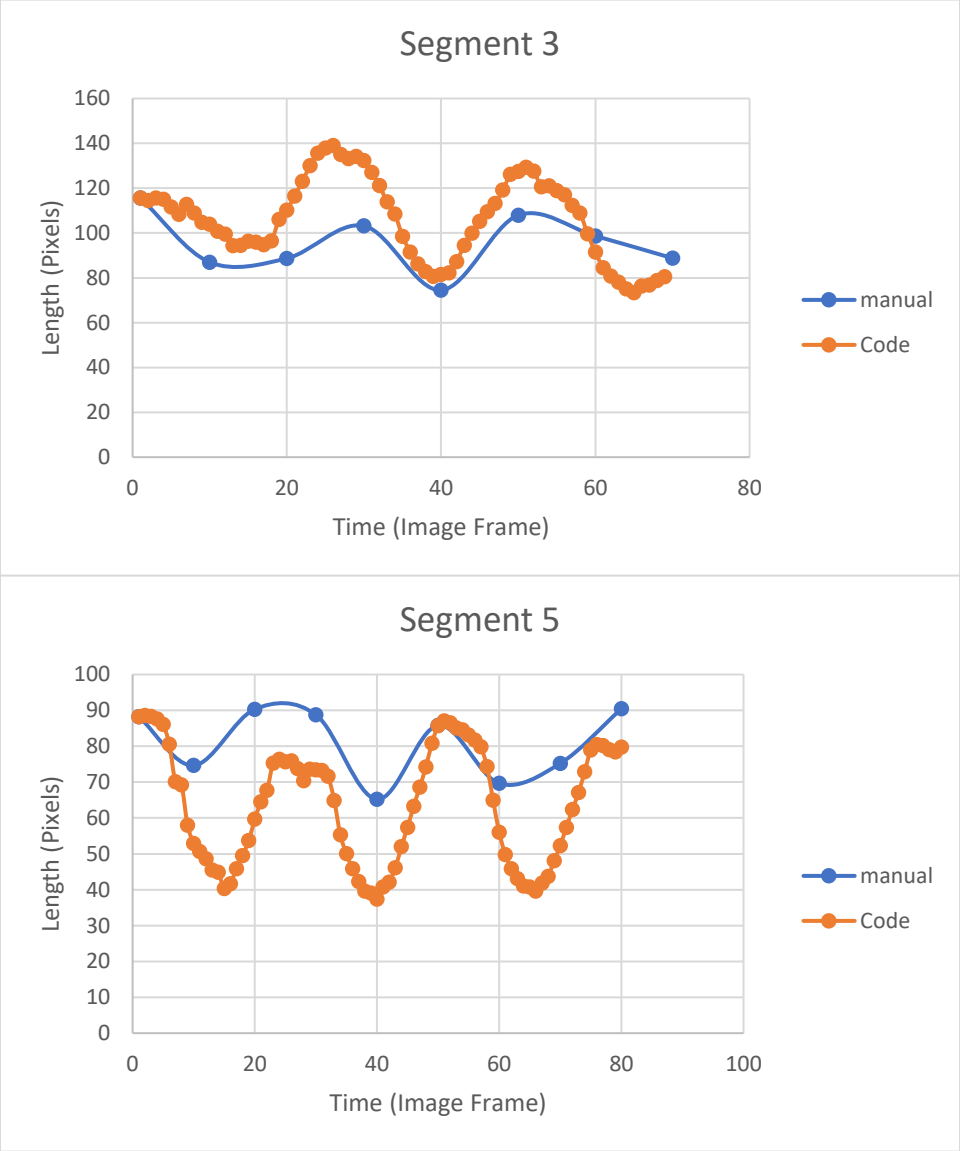
Segment 3
Length (Pixels)
160
140
120
100
80
60
40
20
0
0
20
40
60
80
Time (Image Frame)
manual
Code
Segment 5
Length (Pixels)
100
90
80
70
60
50
40
30
20
10
0
0
20
40
60
80
100
Time (Image Frame)
manual
Code

MI 1

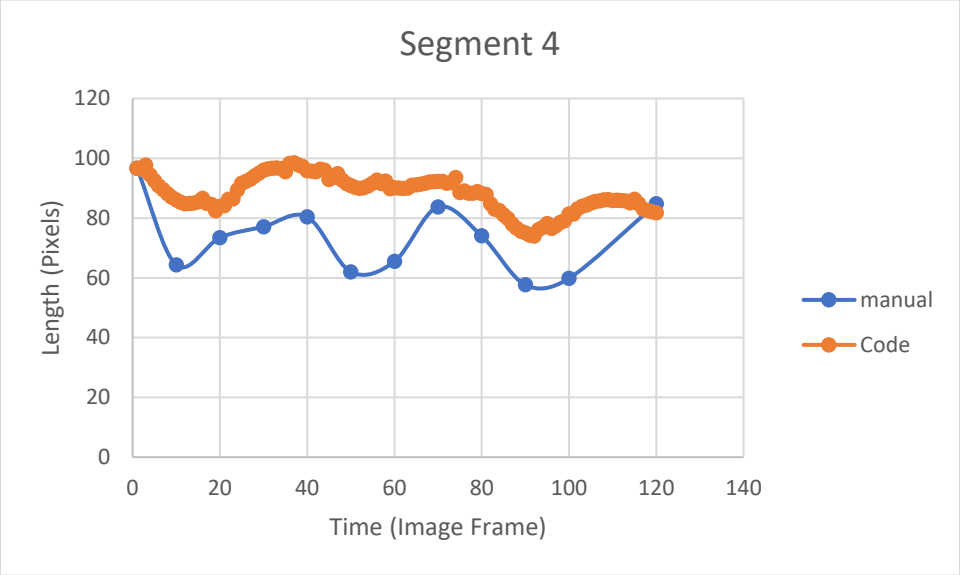
Segment 4
Length (Pixels)
Time (Image Frame)
manual
Code

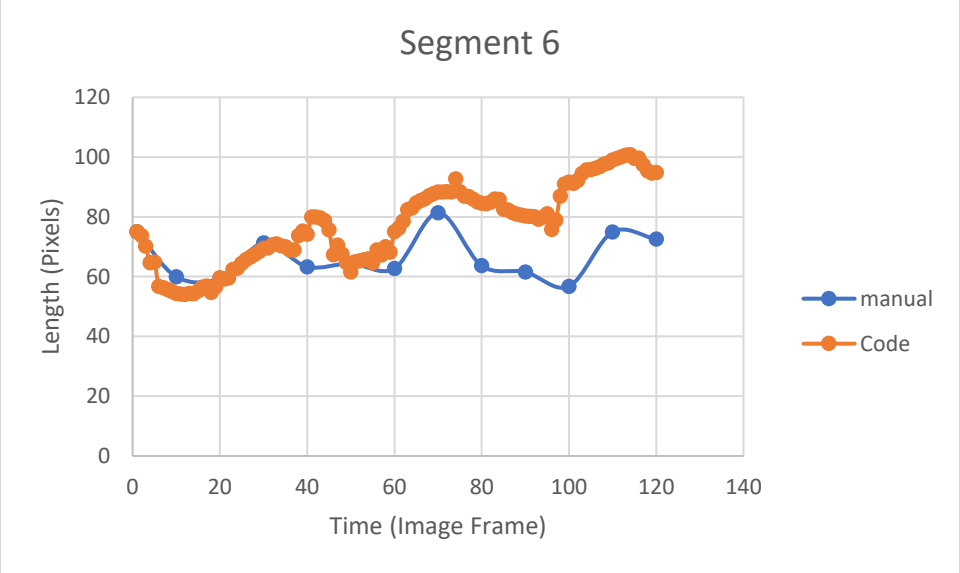
Segment 6
Length (Pixels)
Time (Image Frame)
manual
Code

MI 2

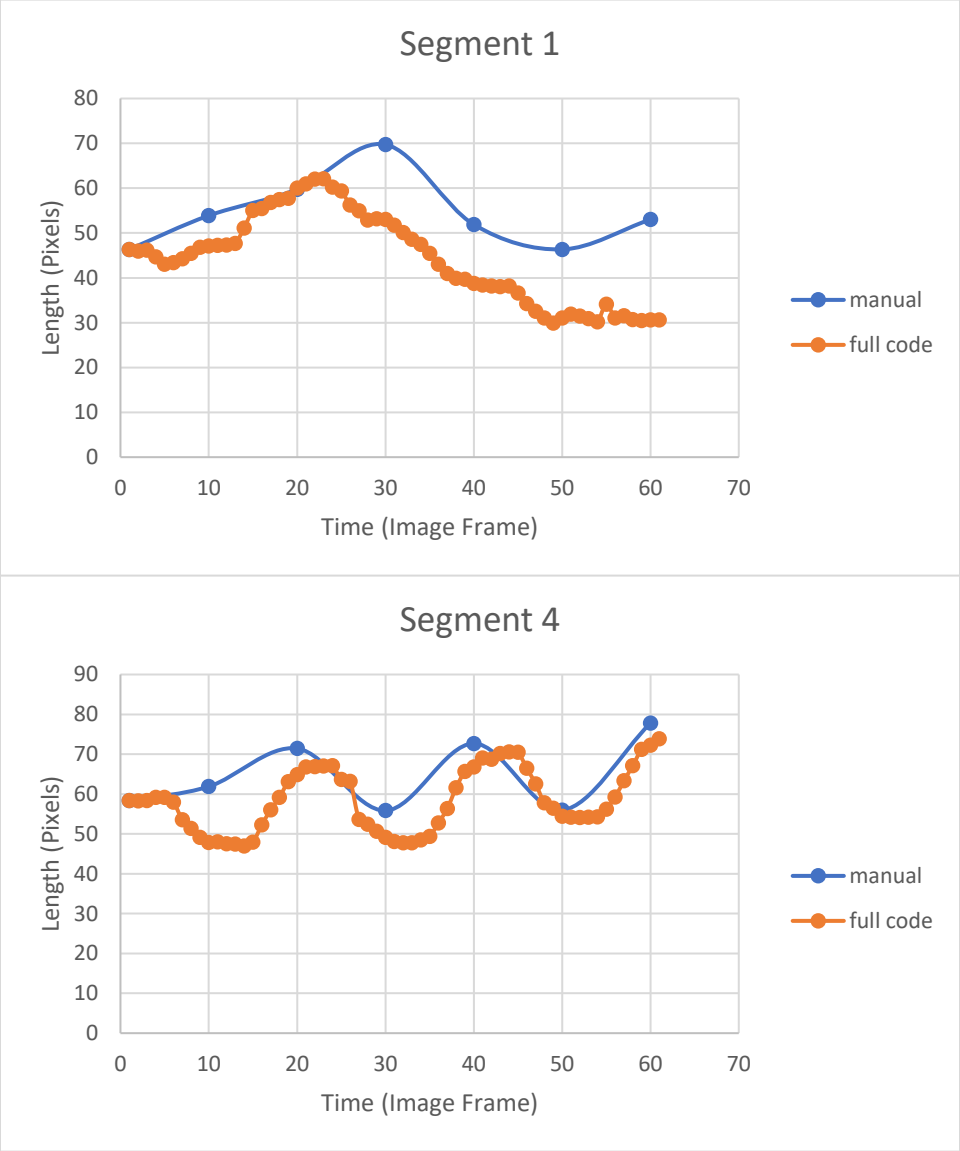
Segment 1
Length (Pixels)
Time (Image Frame)
manual
full code
Segment 4
Length (Pixels)
Time (Image Frame)
manual
full code

MI 3

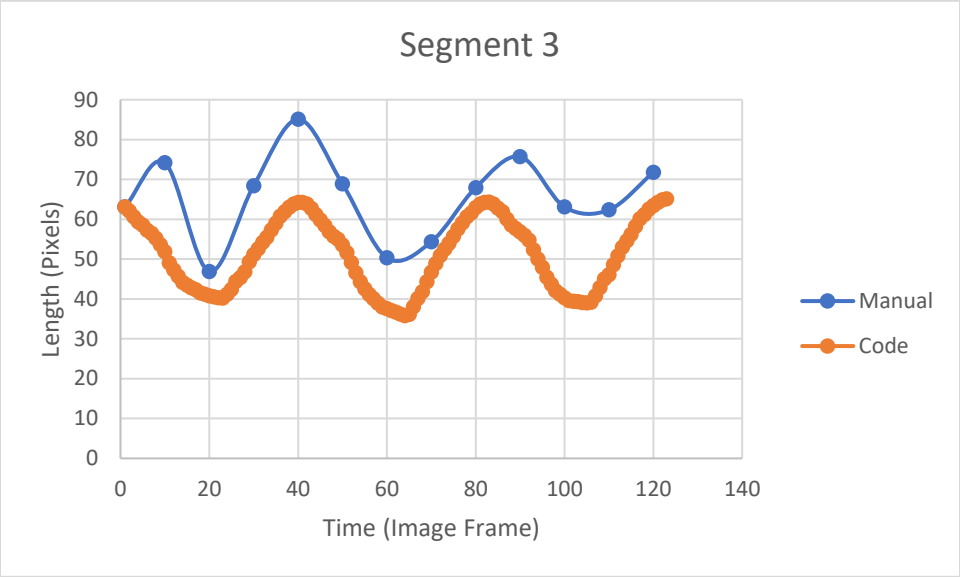
Segment 3
Length (Pixels)
Time (Image Frame)
Manual
Code

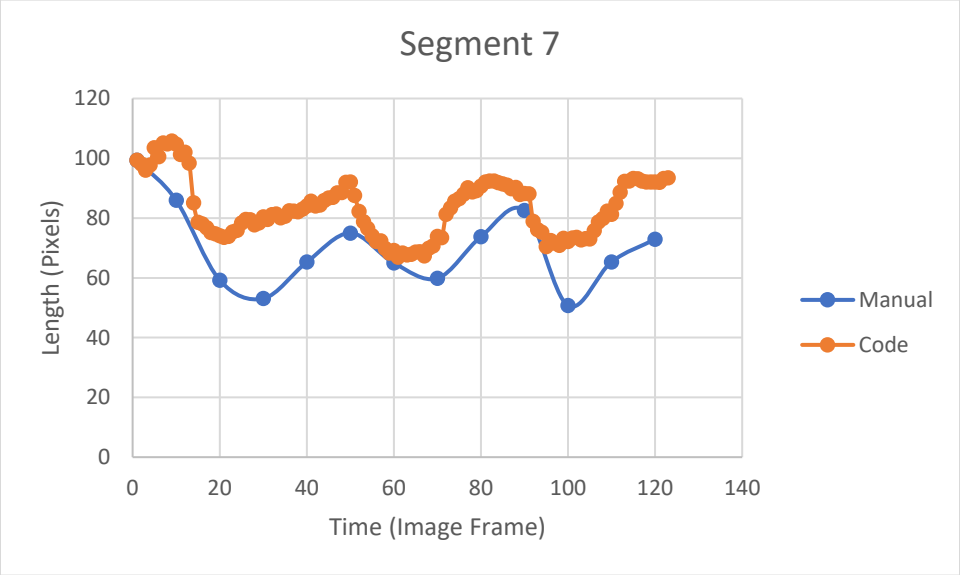
Segment 7
Length (Pixels)
Time (Image Frame)
Manual
Code

Treated 1


Segment 2
Length (Pixels)
Time (Image Frame)
Manual
Code
Segment 10
Length (Pixels)
Time (Image Frame)

Treated 2


Segment 3
250
200
150
100
50
0
Length (Pixels)
0
20
40
60
80
100
Time (Image Frame)
Manual
Code
Segment 8
120
100
80
60
40
20
0
Length (Pixels)
0
20
40
60
80
100
Time (Image Frame)
Manual
Code

Treated 3

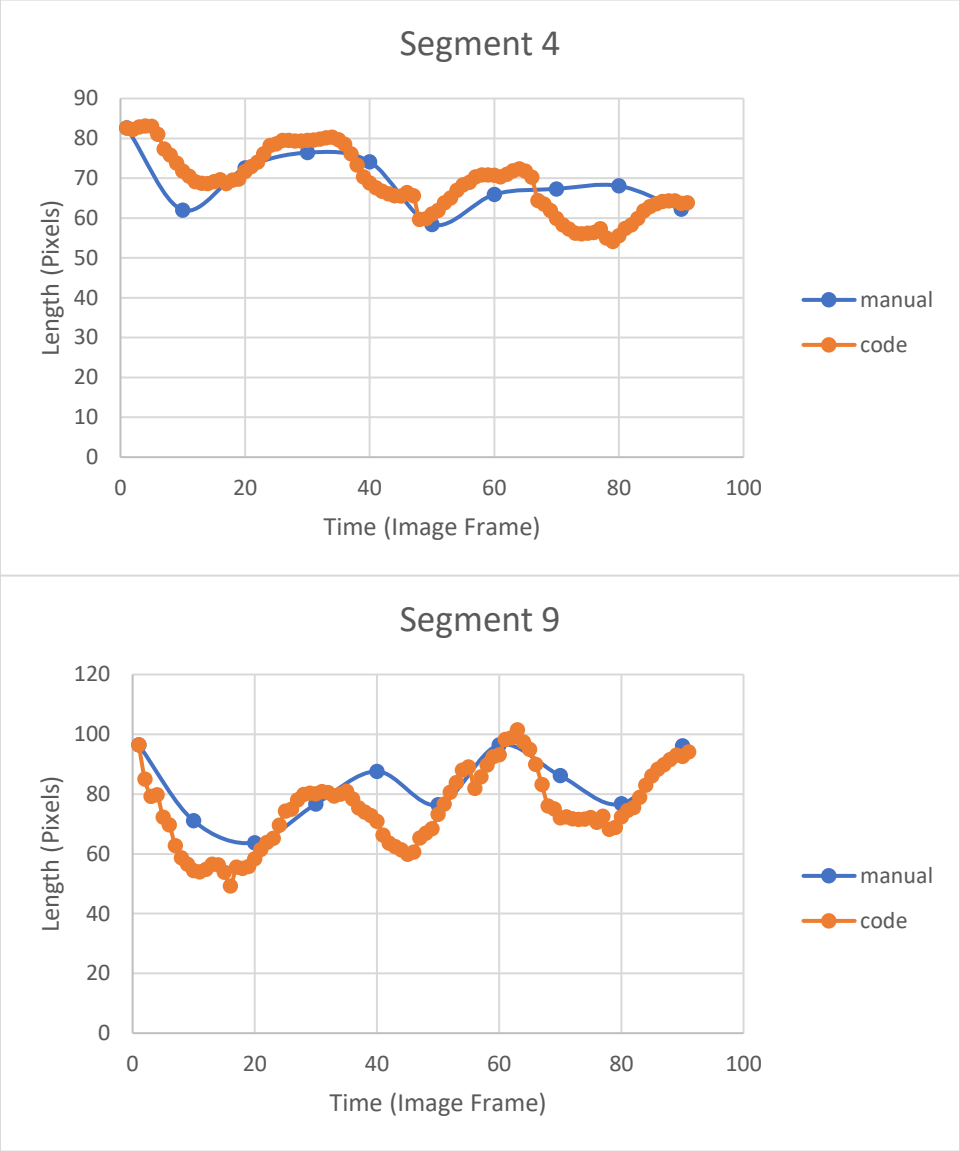
Segment 4
Length (Pixels)
Time (Image Frame)
manual
code
Segment 9
Length (Pixels)
Time (Image Frame)
manual
code

APPENDIX B: Table of Percent Peak Strain Results and Strain Rate Results

			% Peak Strain												
			Segment 1	Segment 2	Segment 3	Segment 4	Segment 5	Segment 6	Segment 7	Segment 8	Segment 9	Segment 10	Segment 11	Segment 12	Global
Code	Sham	S1	123.7346	80.2358	117.6102	257.6206				80.8666	203.8523	271.0671	188.0978	414.9585	193.1160
			101.9852		187.6154				80.8666		237.4597		301.5281		181.8910
		S2	65.4349	74.1362	23.5265	77.2019	36.5489		100.1699	45.1504	26.4802	43.4503	37.1699	60.7652	53.6395
			69.7855		50.3642		36.5489		72.6602		34.9653		48.9676		52.2153
		S3	34.9326	81.7827	56.7254	89.7415	96.1248	97.9484	202.6091	123.1322	32.1843	48.9138	34.0260	45.2446	78.6138
			58.3577		73.2335		97.0366		162.8706		40.5491		39.6353		78.6138
	MI	M1	26.4045		24.0261	15.5979	22.2888	43.6361			153.7690	34.8827	38.1120	19.4410	42.0176
			26.4045		19.8120		32.9625				94.3258		28.7765		40.4563
		M2	43.1916	73.4920	56.8884	44.3723	57.8006	28.3512	154.1232		73.5577	40.9580	42.8472	200.2098	61.5582
			58.3418		50.6304		43.0759		154.1232		57.2578		121.5285		80.8263
		M3	39.1463	56.9307	66.5631	78.2255	48.9640	54.4697	47.5330	63.1816	30.8867	32.2670	39.8676	19.9274	50.7305
			48.0385		72.3943		51.7169		55.3573		31.5768		29.8975		48.1636
	MI + ephrinA1-Fc	T1	72.8448	39.9945	43.9054		120.5918	41.4210		9.4001	10.0916	30.8683	26.1285	104.1586	47.3955
			56.4197		43.9054		81.0064		9.4001		20.4800		65.1435		46.0592
		T2	97.6566		67.8467	160.7424	174.9842	104.3189	230.6492	48.8180	30.2215	26.9709	26.9757	52.8762	92.9146
			97.6566		114.2945		139.6515		139.7336		28.5962		39.9260		93.3097
		T3	39.3101	48.2158	24.5698	30.9349	34.9169	22.6299	22.8065	90.0215	62.0148			20.0258	39.5446
			43.7630		27.7523		28.7734		56.4140		62.0148		20.0258		39.7905
			Segment 1		Segment 2		Segment 3		Segment 4		Segment 5		Segment 6		Global
VevoStrain	Sham	S1	49.6192		37.8563		27.8226		10.6661		29.1688		33.9241		31.5095
		S2	34.2681		29.8271		21.7512		38.8746		24.3630		21.8868		28.4951
		S3	31.6115		31.5130		8.1447		11.5988		36.8732		24.3090		24.0084
	MI	M1	16.2980		9.8318		10.7952		20.5998		11.2097		18.1599		14.4824
		M2	24.7942		26.0929		13.9342		10.9249		24.6237		8.0436		18.0689
		M3	28.2488		18.7205		14.1963		18.4216		35.4987		34.8246		24.9851
	MI + ephrinA1-Fc	T1	26.6301		10.6169		2.9608		0.8529		2.2890		15.6827		9.8387
		T2	19.1708		53.5408		37.3501		27.4865		21.5442		30.1180		31.5351
		T3	12.3862		20.9806		18.9754		-29.4399		29.6035		21.9810		12.4145

% Peak Strain Rate (1/s)																			
			Segment 1		Segment 2		Segment 3		Segment 4		Segment 5		Segment 6		Segment 7		Segment 8		Global
Code	Sham	S1	178.0655	112.9680	93.8223	173.7728								57.4530	121.1092	78.2918	133.1025	697.6583	182.9159
			145.5167		133.7976								57.4530		99.7005		415.3804		170.3696
		S2	60.5261	29.3498	24.6256	26.1199	14.0494					70.0234	38.4734		41.0985	34.4332	36.4124	11.9539	35.1878
			44.9380		25.3727		14.0494					54.2484			37.7659		24.1831		33.4262
		S3	69.7225	54.3147	39.3741	48.7602	60.7426	114.2094				716.6503	108.7827		30.8070	66.6815	45.8779	49.5824	117.1254
			62.0186		44.0671		87.4760					412.7165			48.7442		47.7302		117.1254
	MI	M1	25.5131		15.2112	10.0439	29.0922	32.0362							148.7652	32.0975	33.3279	21.9332	38.6689
			25.5131		12.6275		30.5642								90.4314		27.6305		37.3533
		M2	32.4600	48.4378	34.0271	37.1114	75.9728	29.7070				256.9396			72.5270	51.2937	66.7499	134.6962	76.3566
			40.4489		35.5693		52.8399					256.9396			61.9104		100.7231		91.4052
		M3	16.7255	19.3656	14.8539	18.3656	13.8167	30.6004				25.3559	26.5556		10.3898	8.9500	9.4692	7.8099	16.8548
			18.0455		16.6097		22.2085					25.9557			9.6699		8.6396		16.8548
	MI + ephrinA1-Fc	T1	120.6211	49.4646	57.0586		130.6817	45.3880					20.2955		18.2691	18.3538	12.3924	70.0944	46.8887
			85.0428		57.0586		88.0349					20.2955			18.3115		41.2434		51.6645
		T2	56.3678		56.2687	123.5900	117.0162	87.7624				348.1083	52.2363		62.7994	55.5831	26.4633	39.1072	93.2093
			56.3678		89.9294		102.3893					200.1723			59.1912		32.7853		90.1392
		T3	30.9238	23.7223	13.6786	12.0998	25.8274	52.2007				35.3015	66.0134		36.8657			71.2975	36.7931
			27.3231		12.8892		39.0141					50.6575			36.8657		71.2975		39.6745
			Segment 1		Segment 2		Segment 3		Segment 4		Segment 5		Segment 6		Global				
VevoStrain	Sham	S1	22.3154		17.8148		12.8355		5.1784		10.9051		12.6852		13.6224				
		S2	22.0099		15.2118		17.2951		20.5575		20.3387		13.5792		18.1654				
		S3	18.0158		17.5376		7.0485		9.5293		22.0581		17.8006		15.3317				
	MI	M1	11.7086		9.9417		13.7298		20.3868		6.7759		9.5748		12.0196				
		M2	12.1057		11.9580		7.4151		6.3677		8.9051		7.3800		9.0219				
		M3	10.3079		8.9537		4.0408		4.6221		10.8821		11.2590		8.3443				
	MI + ephrinA1-Fc	T1	16.8155		9.8991		5.6608		4.0182		4.7179		10.8535		8.6608				
		T2	15.0877		33.9618		23.6352		18.3410		13.1852		16.4563		20.1112				
		T3	8.3503		13.2308		14.7715		23.5945		18.5408		9.8278		14.7193				

APPENDIX C: Segmental Strain Comparison across Experimental Groups from Proposed Algorithm

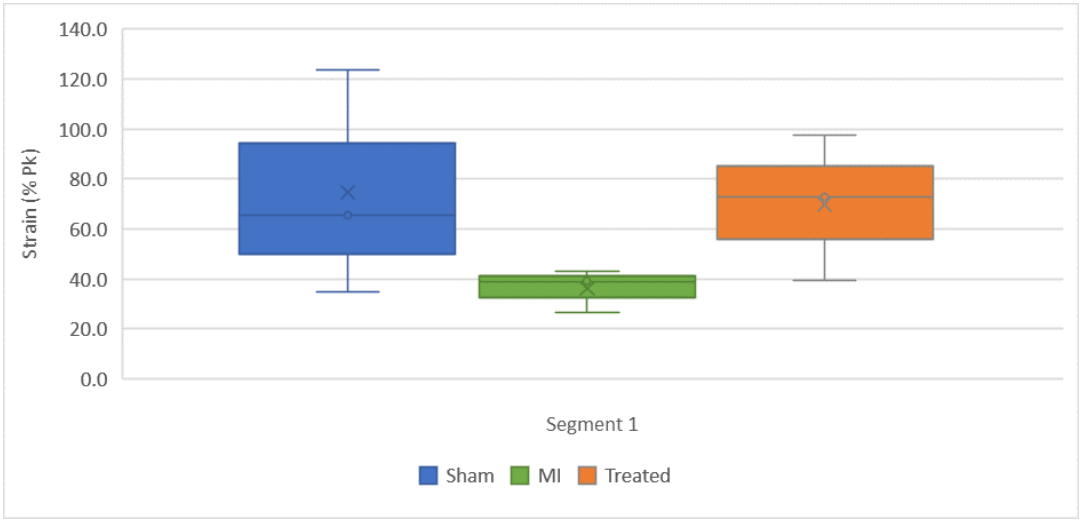

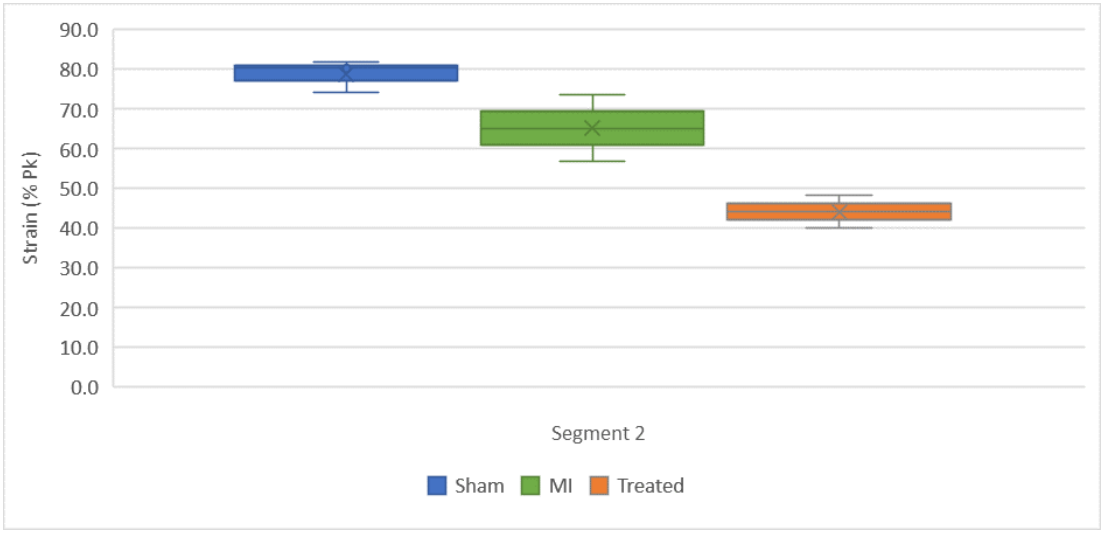

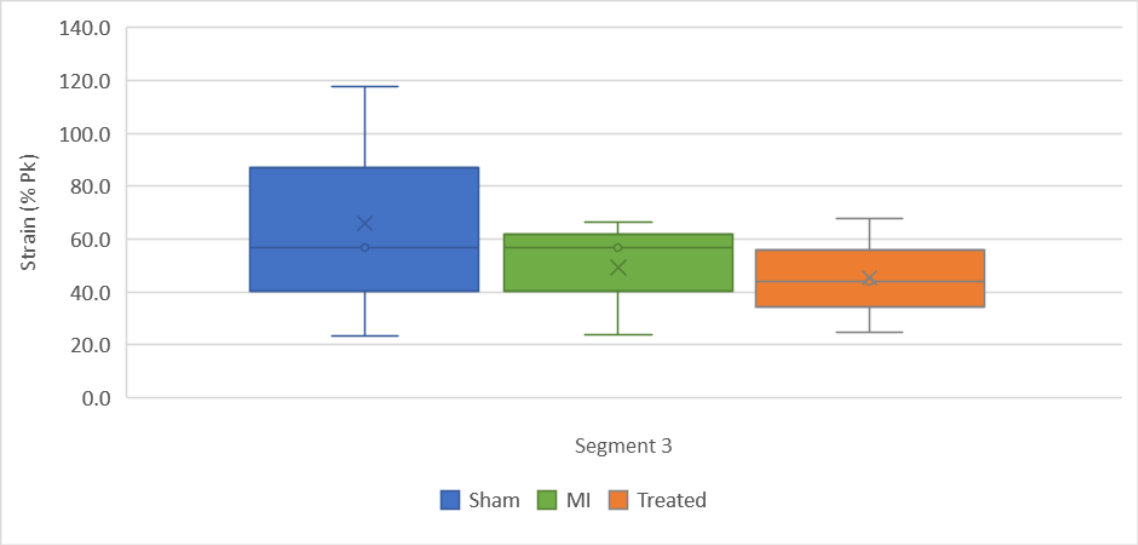
140.0
120.0
100.0
80.0
60.0
40.0
20.0
0.0
Strain (% Pk)
Segment 3
Sham
MI
Treated

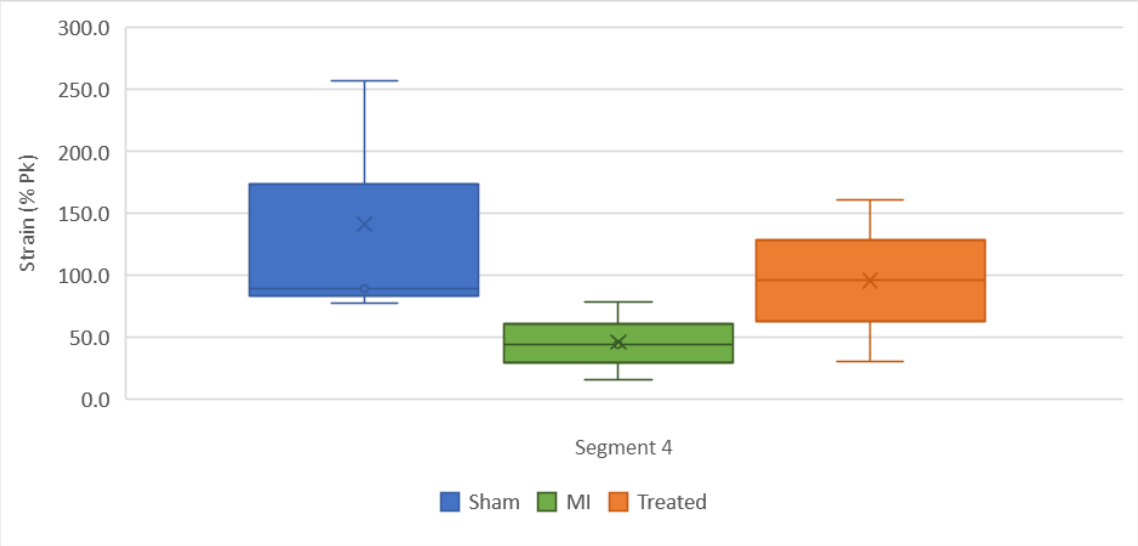
300.0
250.0
200.0
150.0
100.0
50.0
0.0
Strain (% Pk)
Segment 4
Sham
MI
Treated

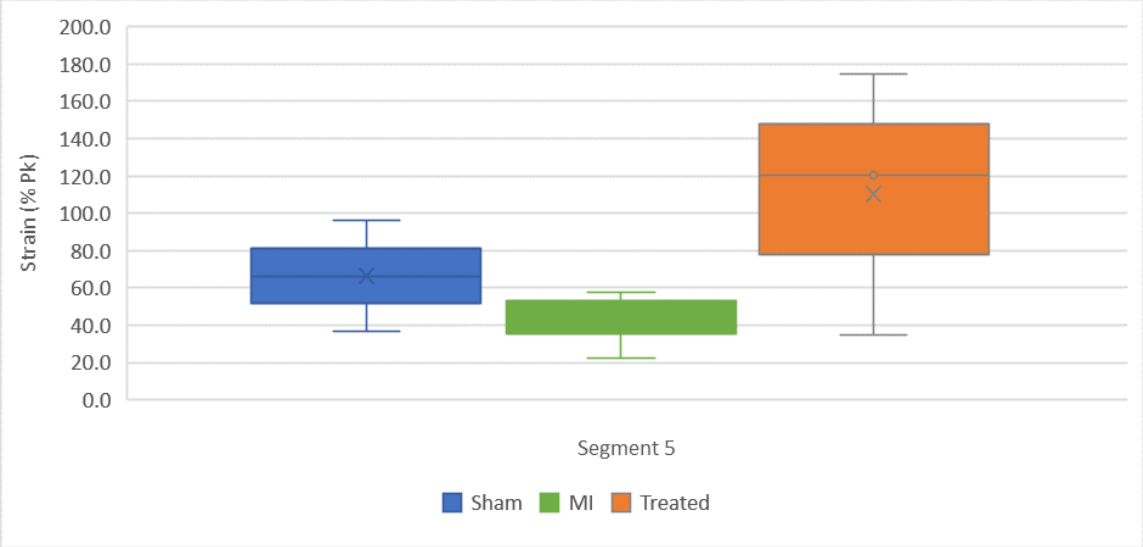
200.0
180.0
160.0
140.0
120.0
100.0
80.0
60.0
40.0
20.0
0.0
Strain (% Pk)
Segment 5
Sham
MI
Treated

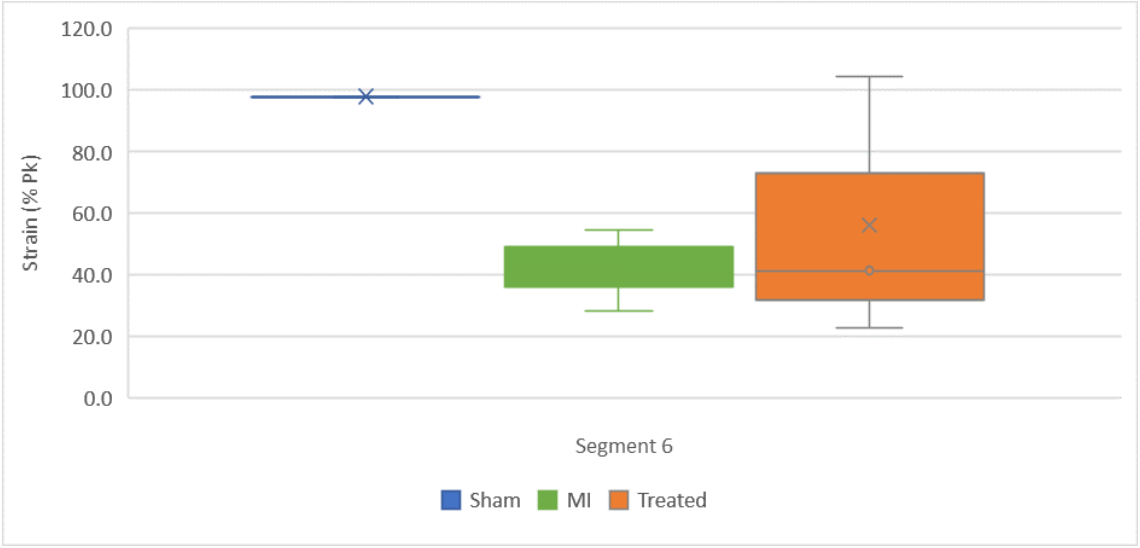
120.0
100.0
80.0
60.0
40.0
20.0
0.0
Strain (% Pk)
Segment 6
Sham
MI
Treated

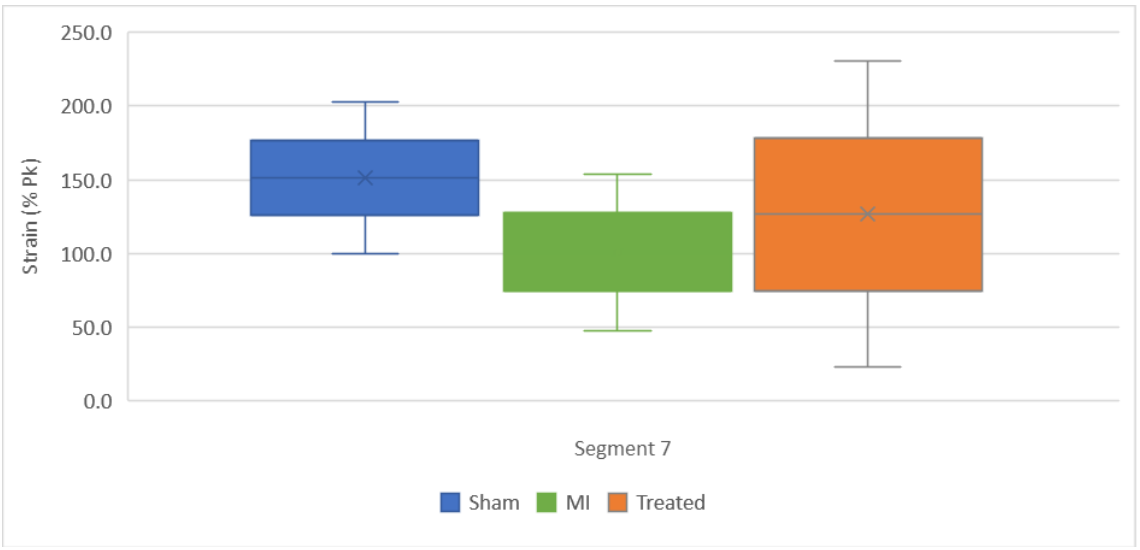
250.0
200.0
150.0
100.0
50.0
0.0
Strain (% Pk)
Segment 7
Sham
MI
Treated

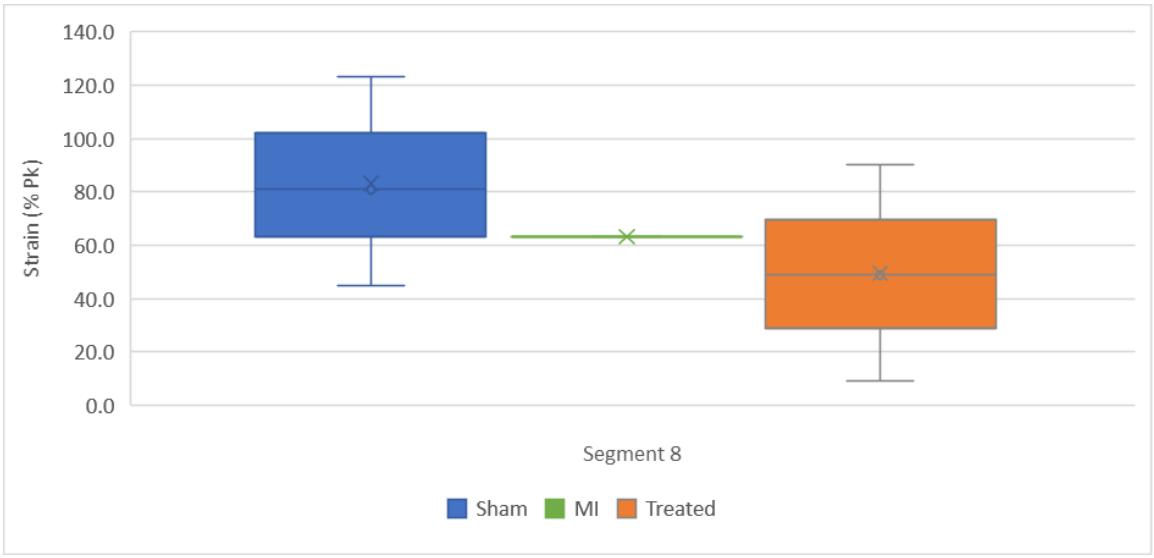
140.0
120.0
100.0
80.0
60.0
40.0
20.0
0.0
Strain (% Pk)
Segment 8
Sham
MI
Treated

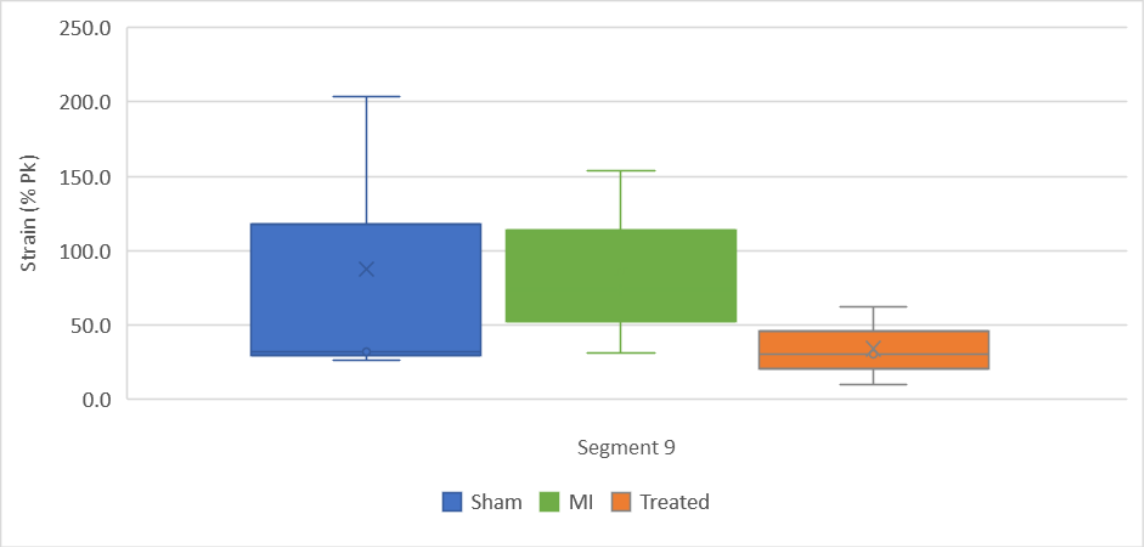
250.0
200.0
150.0
100.0
50.0
0.0
Strain (% Pk)
Segment 9
Sham
MI
Treated

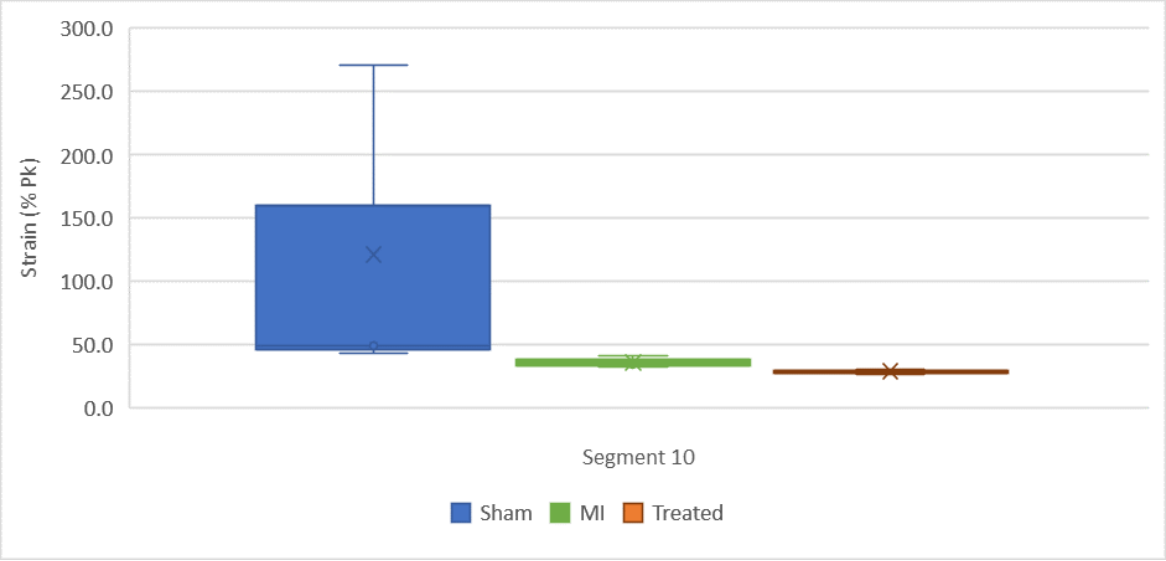
300.0
250.0
200.0
150.0
100.0
50.0
0.0
Strain (% Pk)
Segment 10
Sham
MI
Treated

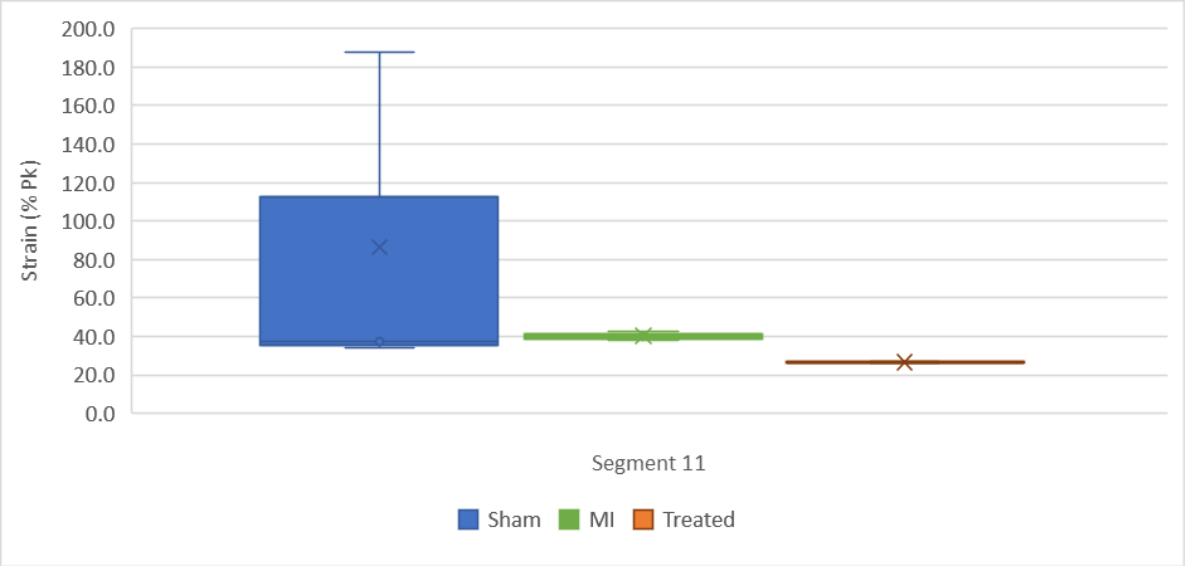
200.0
180.0
160.0
140.0
120.0
100.0
80.0
60.0
40.0
20.0
0.0
Strain (% Pk)
Segment 11
Sham
MI
Treated

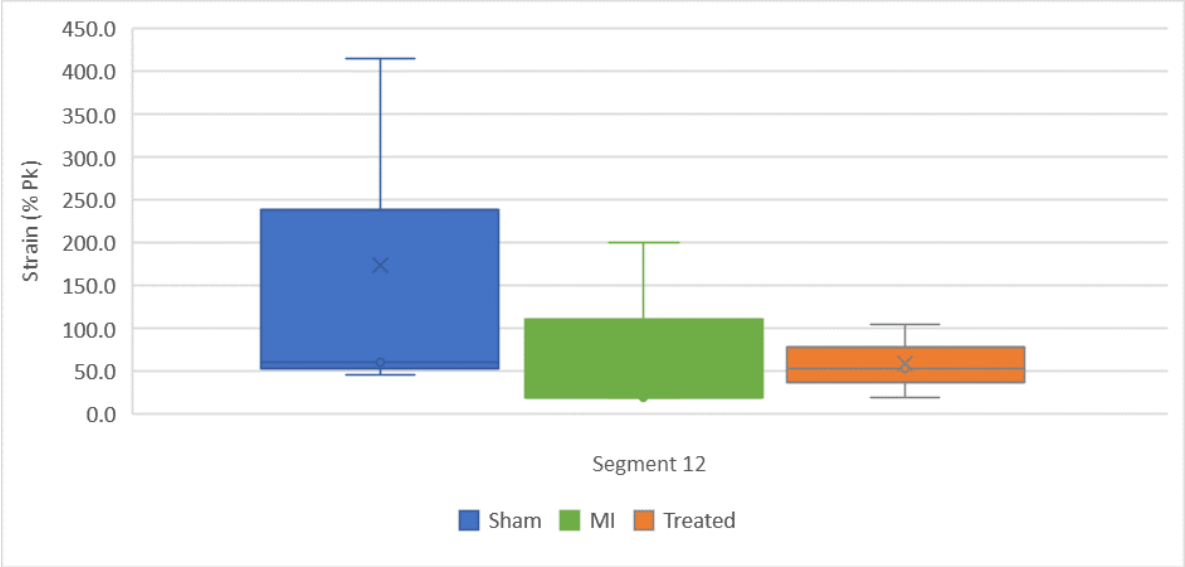
450.0
400.0
350.0
300.0
250.0
200.0
150.0
100.0
50.0
0.0
Strain (% Pk)
Segment 12
Sham
MI
Treated

APPENDIX D: IACUC Approval Form

East Carolina University
Tomorrow starts here.

Animal Care and Use Committee
212 Ed Warren Life Sciences Building
East Carolina University
Greenville, NC 27834-4354

252-744-2436 office
252-744-2355 fax

March 20, 2018

Jitka Virag, Ph.D.
Department of Physiology
EW Life Sciences Building
East Carolina University

Dear Dr. Virag:

Your Animal Use Protocol entitled, "Murine Model of Myocardial Infarct Repair" (AUP #Q228d) was reviewed by this institution's Animal Care and Use Committee on March 20, 2018. The following action was taken by the Committee:

"Approved as submitted"

Please contact Aaron Hinkle at 744-2997 prior to hazard use

A copy is enclosed for your laboratory files. Please be reminded that all animal procedures must be conducted as described in the approved Animal Use Protocol. Modifications of these procedures cannot be performed without prior approval of the ACUC. The Animal Welfare Act and Public Health Service Guidelines require the ACUC to suspend activities not in accordance with approved procedures and report such activities to the responsible University Official (Vice Chancellor for Health Sciences or Vice Chancellor for Academic Affairs) and appropriate federal Agencies. **Please ensure that all personnel associated with this protocol have access to this approved copy of the AUP and are familiar with its contents.**

Sincerely yours,

Susan McRae, Ph.D.
Chair, Animal Care and Use Committee

SM/jd

Enclosure